

to appear in *AJ*, October 1997

Deep *HST* V- and I-Band Observations of Two Globular Clusters in the Halo of M31¹

Stephen Holland, Gregory G. Fahlman, & Harvey B. Richer
 Department of Physics & Astronomy
 #129-2219 Main Mall
 University of British Columbia
 Vancouver, B.C., Canada
 V6T 1Z4

ABSTRACT

We present deep ($V \simeq 27$) V- and I-band stellar photometry of G302 and G312, two globular star clusters in the halo of M31. These data were obtained using the *Hubble Space Telescope*’s Wide Field/Planetary Camera 2. We find iron abundances of $[\text{Fe}/\text{H}] = -1.85 \pm 0.12$ for G302 and $[\text{Fe}/\text{H}] = -0.56 \pm 0.03$ for G312, consistent with spectroscopic measurements. The color–magnitude diagrams for each cluster show no evidence for an intermediate-aged population of stars, or a second parameter effect in the morphology of the horizontal branch. G302 shows no evidence for a color gradient but the inner regions of G312 are bluer than the outer regions. G312 shows no evidence of ellipticity or an extended halo of unbound stars. G302 has a projected ellipticity of $\epsilon = 0.195 \pm 0.012$ with the projected major axis oriented towards the center of M31. G302 also shows evidence of an extended asymmetric stellar halo extending to at least twice the fitted Michie–King tidal radius. The amount of mass beyond the tidal radius of G302 is consistent with the stellar escape rates which have been predicted by *N*-body simulations of globular clusters in the Galactic tidal field.

Subject headings: galaxies: individual (M31) — galaxies: star clusters — stars: luminosity function

1. Introduction

Globular star clusters (GCs) are pressure-supported collections of between $\sim 10^4$ and $\sim 10^6$ stars which are usually associated with galaxies, although there is evidence that some clusters of galaxies contain a population of “free” GCs which are associated with the cluster potential as a whole and not any individual galaxy (West et al. 1995). Individual Galactic GCs are made up of stars with a single overall chemical abundance suggesting that they formed in a single star formation event. GCs typically have integrated magnitudes of $-10 \leq V \leq -4$ making GC systems visible out to redshifts of $z \sim 0.04$, the approximate distance to the Great Wall galaxies. The shape of the GC luminosity function (LF) has been assumed to be universal, so the GC LF has been used as a distance indicator (see Harris 1991 for a review). However,

¹Based in observations with the NASA/ESA *Hubble Space Telescope*, obtained at the Space Telescope Science Institute, which is operated by the Association of Universities for Research in Astronomy, Inc., under NASA contract NAS5-26555.

recent work has suggested that the shape of the GC LF may depend on the metallicity of the GC system (Ashman et al. 1995) and the details of stellar evaporation from individual GCs (Okazaki & Tosa et al. 1995). Because of the wide-spread use of GCs to determine distances to external galaxies, it is important to determine if GCs truly are the same from one galaxy to the next. This is best determined by studying the physical structures and stellar populations of GCs in nearby galaxies.

The nearest large GC system outside the Milky Way Galaxy is that of the Andromeda Galaxy (= M31 = NGC 224). M31 is located at a distance of 725 kpc ($\mu_0 = 24.3$, van den Bergh 1991) so individual stars in M31’s GCs can be easily resolved with the *Hubble Space Telescope* (*HST*) and large ground-based telescopes at sites with sub-arcsecond seeing.

M31’s low inclination ($i = 12^\circ.5$, Hodge 1992) means that many of its GCs are not superimposed against the disk of M31, making identification of GCs, and photometry of their stars, relatively straightforward. M31 offers a unique laboratory to study the outer regions of GCs. Because of their small fields-of-view it is not practical to use CCDs to obtain star counts in the outer regions of Galactic GCs. Beyond distances of approximately half the tidal radius, r_t , the projected stellar densities of the clusters are overwhelmed by random fluctuations in the background stellar number density (Innanen et al. 1983). However, M31’s GCs have sufficiently small angular sizes ($\theta \sim 5''$ to $15''$) that both the cluster and the background can be imaged on a single large format CCD image. This eliminates the need to match photometric zero-points between the cluster and the background, which makes possible a more precise subtraction of the background light from the cluster light.

The first study of the internal structures of M31 GCs was undertaken by Battistini et al. (1982), who estimated core radii for several clusters. Pritchet & van den Bergh (1984) found that the surface brightness profile for G1 (= Mayall II; the G-numbers used in this paper are from Sargent et al. [1977]) had an excess of light at large radii compared to the best-fitting seeing-convolved analytical King (1966) model. They did find that G1 was well fit by empirical King (1962) models with core radii of $r_c \lesssim 0.5$ pc. Crampton et al. (1985) used seeing-convolved King (1962) models to derive core radii for nearly 500 M31 GCs. Their values, however, are systematically $\sim 50\%$ larger than those of Battistini et al. (1982), despite the better seeing conditions of the Crampton et al. (1985) data set. Bendinelli et al. (1990) used ground-based data to produce seeing-deconvolved radial profiles for six bright GCs in M31, but seeing and pixel scale limitations restricted them to resolutions of $\sim 0''.3$, insufficient to resolve the cores of the clusters. Still, their data suggest that M31 GCs have King-like profiles similar to those of Galactic GCs.

The core structures of some of M31’s GCs have been studied using the pre-refurbished *HST*. Bendinelli et al. (1993) detected a power-law density cusp in G105 using *HST*’s Faint Object Camera (FOC) images and a variety of image restoration and seeing deconvolution techniques. In addition, Fusi Pecci et al. (1994) used similar methods to obtain half-width at half-maxima (HWHM) and half-light radii (r_h) for thirteen M31 GCs from FOC images. They found HWHMs similar to the core radii of Galactic GCs. Their data, however, could not be used to find the tidal radii of these clusters because the point-spread function (PSF) before the refurbishment of the *HST* overfilled the FOC’s field of view.

Cohen & Freeman (1991) derived tidal radii for thirty M31 GCs by fitting seeing-convolved King models. Although their fits to individual clusters were quite uncertain they did find a mean tidal radius for the M31 clusters—after adjustment for differences in galactic masses and rotation velocities—which was very similar to that of the Milky Way clusters. GCs do not exist in isolation but sit in the tidal field of a galaxy. Any stars that evaporate from a GC by the galaxy will have velocity vectors similar to the velocity vector of the GC. This can result in the GC being surrounded by an extended halo of unbounded stars

which move in approximately the same direction as the GC and have approximately the same velocity. This idea has been explored numerically by Oh & Lin (1992) who predicted that GCs could be surrounded by extended halos of escaped stars which can persist for up to a Hubble time. The size and shape of such a halo can be influenced by the tidal field of the parent galaxy. Evidence for extended halos has been observed in some Galactic GCs by Grillmair et al. (1995). In addition, Grillmair et al. (1996, hereafter referred to as GAF) have observed an excess of resolved and unresolved stars beyond the formal Michie–King (MK) tidal radii of several GCs in M31, as would be expected if extended halos were present.

There has been some interest in determining the ellipticities of M31 GCs. Pritchett & van den Bergh (1984) measured an ellipticity of $\epsilon = 0.22$ for the region of G1 with $12'' \lesssim r \lesssim 35''$. Spassova et al. (1988) measured ellipticities for approximately two dozen GCs while a study by Lupton (1989) suggests that the mean ellipticity measured in the inner 7 to 14 pc of a M31 GC ($\bar{\epsilon} = 0.08$) is indistinguishable from the mean ellipticity of Galactic GCs. In the outer 14 to 21 pc, however, the mean ellipticity of an M31 cluster is 0.11 ± 0.08 , greater than that of the Galactic GCs ($\bar{\epsilon} = 0.08 \pm 0.07$) and similar to GCs in the Large Magellanic Cloud ($\bar{\epsilon} = 0.11 \pm 0.07$). Baev et al. (1997) found systematic differences between the shapes of M31’s disk and halo GCs. They found that the disk GCs are triaxial ellipsoids while the halo GCs are oblate or prolate spheroids, but cautioned that this is a preliminary result since the sample of halo GCs in their study is small compared to the sample of disk GCs.

The first color–magnitude diagrams (CMDs) for GCs in M31 were for G1 by Heasley et al. (1988) and G219 (= Mayall IV) by Christian & Heasley (1991). Couture et al. (1995) undertook a systematic study of five M31 GCs (G11, G319, G323, G327 = Mayall VI, and G352 = Mayall V) with a range of iron abundances. Unfortunately none of these ground-based studies were able to reach the level of the horizontal branch (HB) at $V \simeq 25$. The first CMDs constructed from *HST* data were for G1 (Rich et al. 1996); G58, G105, G108, and G219 (Ajhar et al. 1996); and G280, G351, and Bo468 (Fusi Pecci et al. 1996). These CMDs were able to resolve stars one to two magnitudes below the red portion of the HB.

In order to study the stellar populations and structures of GCs in M31 we obtained deep *HST* Wide-Field/Planetary Camera-2 (WFPC2) images of two halo GCs (G302 and G312) located $32''.1$ and $49''.8$ respectively from the center of M31 along the southeast minor axis. Our data is unique in that we have centered the GCs on the WF3 CCD in order to take advantage of the WFC’s field of view to search for extended halos around each GC.

2. Observations and Data Reductions

2.1. Observations

We obtained deep *V*- and *I*-band images of two bright GCs, G302 ($\alpha_{2000.0} = 00^{\text{h}}45^{\text{m}}25^{\text{s}}.2$, $\delta_{2000.0} = +41^{\circ}05'30''$) and G312 ($\alpha_{2000.0} = 00^{\text{h}}45^{\text{m}}58^{\text{s}}.8$, $\delta_{2000.0} = +40^{\circ}42'32''$) in the halo of M31. These data were obtained using the *HST* in cycle 5 program #5609. We used the WFPC2 operating at -88°C with a gain setting of $7 \text{ e}^-/\text{ADU}$.

Table 1 lists the exposures obtained in each filter. Exposure times were based on the central surface brightnesses of the two GCs as determined from ground-based observations (Holland et al. 1993, Holland 1997) and chosen to avoid saturating the cores of the GCs. The total exposure times were 4320 seconds in the F555W (WFPC2 broadband *V*) filter and 4060 seconds in the F814W (WFPC2 broadband *I*) filter for each field. The data was pre-processed through the standard STScI pipeline for WFPC2 data. Known bad

pixels were masked, and geometric corrections were applied using standard techniques.

G302 is located $32'.1$ from the center of M31 (a projected distance of $R_{\text{M31}} = 6.8$ kpc) approximately along the southeast minor axis while G312 is located $49'.8$ from the center of M31 ($R_{\text{M31}} = 10.5$ kpc) approximately along the southeast minor axis. Each GC was centered on the WF3 CCD. We chose to locate the GCs on the WF3 CCD, instead of taking advantage of the higher spatial resolution offered by the smaller pixels of the PC CCD, for three reasons:

First, the tidal radii of G302 and G312, as determined by fitting MK models (Michie 1963, King 1966) to the surface brightness profiles of G302 and G312 derived from HRCam observations taken at the CFHT, are $r_t \simeq 10''$ (Holland et al. 1993, Holland 1997). Therefore, each GC would occupy a significant fraction of the total field of view of the PC, leaving insufficient area to make reliable determinations of the spatial variations in the background stellar density.

Second, Grillmair et al. (1995) found evidence for extended stellar halos, extending to ~ 2 to 3 times the tidal radius, in several Galactic GCs. Recently, GAF and Holland (1997) found weak evidence for stellar density enhancements out to $\sim 2r_t$ in some M31 GCs including G302 and G312. By centering the GCs on the WF3 CCD we ensured that as much as possible of any extended halos would be located on the same CCD as the GC itself. This enabled us to avoid systematic effects that may occur if surface brightness and stellar number density data are transferred between the PC and WFC CCDs, with their different pixel scales and sensitivities.

Third, by locating the GCs at the center of the WF3 CCD we were able to use the WF2 and WF4 CCDs to probe the stellar populations in the halo of M31. These results are published in Holland et al. (1996, hereafter referred to as HFR). Having two background fields for each GC field enables us to differentiate between stellar number-density enhancements that are due to statistical fluctuations in the star counts from M31 halo stars, and those that are due to physical structures, such as extended halos of unbound stars, that are related to the GCs.

2.2. Data Reductions

Photometry was performed on stars imaged by the WFPC2's Wide Field CCDs using the DAOPHOT II/ALLFRAME software (Stetson 1987, Stetson 1994). All nineteen images for each field were re-registered to a common coordinate system and median-combined. This eliminated cosmic ray hits and increased the signal-to-noise ratio (S/N) in our data allowing fainter stars to be detected. In order to eliminate large-scale gradients in the images due to unresolved light from the GCs (the gradient in the light from the halo of M31 was $\lesssim 1\%$ in both the G302 and G312 fields) a square median-filter was run over the combined image to produce a map of the large-scale gradients. This smoothed image was then subtracted from the combined image and a constant sky added back to produce a median-subtracted image. The size of the square median-filter was ~ 5 times the stellar full-width at half-maximum (FWHM) to avoid smoothing out structure in the stellar images (e.g. Stetson & Harris 1988). Subtracting the median-filtered image resulted in a reasonably clean subtraction of the integrated light from each GC to within ~ 25 pixels ($\simeq 2''.5 \simeq 9$ pc) of the center of each GC. This process is the digital equivalent of unsharp masking.

The DAOPHOT FIND routine, with a FIND threshold of $7.5\sigma_{\text{sky}}$, was used to detect peaks on the median-subtracted image. We experimented with different FIND thresholds and found that $7.5\sigma_{\text{sky}}$ excluded most of the mis-identifications of noise spikes and cosmic-ray events as stars at faint magnitudes while

including almost all of the stars to the photometric limit of the data. FIND was able to reliably detect stars to within ~ 25 pixels ($\sim 2''.5$) of the center of each GC. Artificial star tests showed that detections closer to the centers of the GCs than this were usually spurious.

The resulting list of stellar candidates was used as input to ALLFRAME. ALLFRAME does simultaneous PSF fitting on all the *original* images (*not* the combined median-subtracted image) to preserve the photometric properties of the data. The PSFs used (Stetson 1996) were Moffatians (Moffat 1969) with $\beta = 1.5$ and a look-up table of residuals. The PSFs varied quadratically over each CCD to account for variations in the form of the PSF from one part of the CCD to another. Only stars which appeared in at least seven frames for each filter were considered to be real stars. Tests with different minimum numbers of frames showed that this requirement provides a clean CMD without significantly affecting the limiting magnitude.

Aperture corrections and photometric calibrations were performed in exactly the same manner as described in HFR. We adopted a distance modulus of $\mu_0 = (m - M)_0 = 24.3 \pm 0.1$, a reddening of $E_{V-I} = 0.10 \pm 0.03$, and interstellar extinctions from Tables 12A and 12B of Holtzman et al. (1995). These extinction values are dependent on the stellar spectrum. For a K5 giant the extinctions were $A_V = 0.320$ and $A_I = 0.190$. See HFR for a discussion of why these values were adopted. Table 2 lists the adopted aperture corrections for the WFPC2 CCDs. We were unable to obtain reliable aperture corrections for the PC images of the G312 field due to a lack of bright stars in this field. Photometry in this field exhibited an unusually high degree of scatter, although the stellar images appeared to be normal to the eye. As a result, we have not included this data in any of the analysis presented here.

ALLFRAME's χ statistic represents the ratio of the observed pixel-to-pixel scatter in the PSF fitting residuals to the expected amount of scatter given the noise properties of the data. Values of χ which are significantly greater than unity indicate that the image was not well fit by the stellar PSF and thus may not be a star. In light of this we discarded any stars with a final χ value of greater than 2. In order to eliminate stars with poorly determined magnitudes we used an interactive approach based on the uncertainty in the calibrated magnitude. A plot of uncertainty vs. magnitude was made and a locus defined which corresponded to the expected photometric scatter at a given magnitude. Any stars which were judged to have a significantly greater uncertainty than the typical value for that magnitude were discarded. Visual examinations of the CMDs and the WF images suggested that we did not remove any legitimate stars from our sample. We wish to stress that this culling was done *solely* on the basis of the photometric uncertainty of each star, not on the star's location on the CMD or the CCD. Mean photometric uncertainties for our entire culled data set are listed in Table 3 of HFR. The mean photometric uncertainties, based on the formal photometric uncertainties returned by DAOPHOT II/ALLFRAME, for the GC stars are listed in Table 7 of this paper.

The complete set of calibrated stellar photometry for G302 and the surrounding fields is listed in Table 3. The photometry for G312 and its surrounding fields (with the exception of the PC field) is listed in Table 4. Column (1) gives the CCD the star was observed on. Column (2) gives an identification number for each star. The identification numbers are only unique for stars on a given CCD. Columns (3) and (4) give the location of the star on the CCD in pixel coordinates. Column (5) is the *V*-band magnitude, column (6) the $1\text{-}\sigma$ uncertainty in the *V*-band magnitude, and column (7) is the value of the DAOPHOT χ statistics. Columns (8) to (10) are the same as columns (5) to (7) except they give values for the *I*-band. Tables 5 and 6 list the photometry for stars with $r \leq 10''$ of the center of G302 and G312. The data is the same as for Tables 3 and 4 except an extra column, giving the distance of the star from the center of the GC, has been added. Only the first ten lines of Tables 3, 4, 5, and 6 are published here. The full tables can

be found on the AAS CD-ROM Volume 9. A total of 12,289 stars were found in the three G302 WFC fields while 3,355 stars were found in the three G312 WFC fields. There are 626 stars within $10''$ of the center of G302 and 325 stars within $10''$ of the center of G312.

2.3. Artificial Star Tests

In order to determine the effects of crowding, as well as the efficiencies of our star-finding and photometry techniques, on our photometry, we undertook a series of artificial star tests. We used the following procedure to generate and recover artificial stars:

1. For each field we generated a series of artificial stars with $(V, (V - I))$ colors based on the observed CMD and LF of the M31 halo stars.
2. The artificial stars were added to each of the original images for a field. The total number of artificial stars added in each field was $\sim 10\%$ of the total number of stars in that field.
3. The entire photometry process described in Sec. 2.2 (FIND/ALLFRAME/culling/matching) was performed on this new set of images and the resulting photometry was matched against the original list of artificial stars for that field.
4. This process was repeated until we had recovered approximately the same number of artificial stars as there were real stars found on that CCD.

This process was performed for each CCD field.

Figure 1 shows the relationship between the input magnitudes of the artificial stars and their recovered magnitudes for a typical set of stars, in this case using the WF2 field near the GC G312. Artificial stars with magnitude differences of more than $\pm\Delta V = 1$ mag have been omitted. This figure plots the magnitude difference as a function of the recovered, not the input, magnitudes of the artificial stars. This was done because the observed magnitudes of the real stars are the recovered magnitudes, not the actual (or input) magnitudes. Therefore, Figure 1 can be used to directly determine the uncertainty in a star’s observed magnitude. Kolmogorov–Smirnov (KS) tests show that the distributions of recovered magnitudes for the artificial red-giant branch (RGB) and HB stars are the same at the 98.892% confidence level in the V -band and at the 99.999% confidence level in the I -band. The apparent excess scatter in the HB artificial stars is merely an artifact of the large number of artificial HB stars.

Table 8 lists the systematic shifts in V and $(V - I)_0$ as well as the degree of scatter as a function of magnitude for the artificial red-giant branch (RGB) stars of G312. Table 9 lists these quantities for the G312 artificial HB stars. In these tables the notation $[x]$ indicates the median value of the individual x_i values. The columns are (1) the boundaries of the bin, (2) the median recovered magnitude, $[V]$; (3) the median photometric uncertainty in the recovered magnitudes (from DAOPHOT), $[\sigma_V]$; (4) the median magnitude difference, $[\delta_V] \equiv [V_{\text{recovered}} - V_{\text{input}}]$; (5) the amount of scatter present in the artificial stars in that bin, $\hat{\sigma}_V \equiv [|\delta_V - [\delta_V]|]$; columns (6) to (9) are the same quantities for the $(V - I)_0$ color; and (10) is the number of artificial stars in that bin. These quantities are identical to those described by Stetson & Harris (1988) except for $\hat{\sigma}$, which we defined in non-parametric terms instead of in Gaussian terms.

Our reduction process has a slight tendency to underestimate the brightnesses of stars near the photometric limit of our data (see column 4 of Table 8). However, this systematic shift is less than the

internal scatter in the photometry and is smaller than ~ 0.05 mag for RGB stars at the level of the HB. Therefore, we conclude that the systematic uncertainties in our photometric reductions do not affect the morphology of the CMDs above $V \sim 26$.

Figure 2 shows a CMD created from a set of artificial RGB stars added to the G312 WF3 image. The HB stars have been omitted in order to show the increase in the scatter in the recovered colors at fainter magnitudes. The amount of scatter seen at a particular magnitude is comparable to the amount of scatter seen in the CMD of G312, which is believed to be made up of stars with a single metallicity. If the stellar populations in M31 GCs are analogous to the stellar populations in Galactic GCs, then the observed spread in G312’s RGB is primarily due to photometric uncertainties. Figure 2 shows that photometric uncertainties are sufficient to explain all the observed width of the RGB of G312.

Table 9 and Figure 3 show that HB stars, because of the large color spread in the HB, can suffer badly from systematic differences between their input and recovered magnitudes. Blue HB stars are scattered by as much as 0.5 mag. in $(V - I)_0$, while red HB stars have a tendency to be recovered at fainter magnitudes and redder colors than they really are. This tends to move red HB stars into the lower half of the RGB resulting in our star counts underestimating of the total number of red HB stars in the GC. The artificial star tests show that stars from the red and blue sides of the HB can be scattered into the RR Lyrae gap. This making it difficult to distinguish RR Lyrae candidates from stars which have simply scattered into the RR Lyrae gap.

3. The Color–Magnitude Diagrams

3.1. Contamination

There are four possible sources of contamination in the CMDs of the GCs. The first three—Galactic halo stars, background galaxies, and M31 disk stars—are discussed in Sec. 3.1 of HFR. By scaling those results to the area on the sky covered by each GC we estimate that at most 15 ± 4 of the objects with $V \leq 24$ in each of Figures 4 (G302) and 6 (G312) are due to contamination from these three sources.

The fourth source of contamination is the halo of M31 itself. To estimate the number of halo stars that should be visible in the CMD for each GC we computed the stellar surface densities in the WF2 and WF4 CCDs for each field. These CCDs were centered $\sim 75''$ from the center of the WF3 CCD (and thus the GCs). Since G302 and G312 have tidal radii of $\sim 10''$ the WF2 and WF4 CCDs will not suffer from contamination from GC stars. The mean background for M31 halo stars with $V \leq 24$ near G302 is $\Sigma_{\text{bkgd}} = 0.0654 \pm 0.0024$ stars/ \square'' , corresponding to 20 ± 5 halo stars in the RGB for G302. Near G312 the background is $\Sigma_{\text{bkgd}} = 0.0174 \pm 0.0012$ stars/ \square'' , corresponding to 5 ± 1 stars in the RGB of G312. These estimates are reasonably consistent with the numbers of objects in the upper halves of Figures 4 and 6 that do not fall on either the RGB or the asymptotic-giant branch (AGB) of each GC.

On the basis of these calculations we expect that contaminating objects make up $\lesssim 7\%$ of the objects in the G302 CMD. Similarly contaminating objects make up $\lesssim 16\%$ of the objects in the G312 CMD. These numbers are consistent with the number of discrepant objects in each CMD so we conclude that the morphologies of the CMDs in Figures 4 and 6 are real and not due to contamination.

3.2. G302

Figure 4 shows the CMD for the GC G302. Stars located between $2''.5 \leq r \leq 10''$ from the center of the cluster are shown. The $r = 10''$ cut-off approximately corresponds to the tidal radius of the GC while the $r = 2''.5$ cut-off is the point where extreme crowding conditions make it impossible to obtain reliable stellar photometry. To estimate the metallicity of G302 we took the dereddened fiducial RGB sequences for several Galactic GCs (from Da Costa & Armandroff 1990, hereafter referred to as DCA), shifted them to the distance of M31 ($\mu_0 = 24.3$), and overlaid them onto Figure 4. The lack of a turn-over at the top of the G302 RGB is consistent with a metal-poor population with an iron abundance of $[\text{Fe}/\text{H}] \simeq -1.5$ to -2.2 . We interpolated between the DCA fiducial sequences to obtain $[\text{Fe}/\text{H}] = -1.85 \pm 0.12$ for G302, where the uncertainty is one-third of the spread in the RGB and corresponds to approximately one standard deviation if we assume the spread in the RGB is due to normally distributed errors in the photometry. Our estimate of the iron abundance for G302 agrees with spectroscopic estimates by Huchra et al. (1991, hereafter referred to as HBK), $[\text{Fe}/\text{H}] = -1.76 \pm 0.18$, and de Freitas Pacheco (1997), $[\text{Fe}/\text{H}] = -1.80 \pm 0.2$.

AGB stars in G302 can be seen to the blue of the low-metallicity fiducial sequences in Figure 4. Unfortunately the AGB and the RGB blend together so it is not possible to unambiguously distinguish AGB stars from RGB stars. This is due to photometric scatter ($\sigma_{V-I} \simeq 0.06$ at $V = 23$) and contamination from RGB stars in the halo of M31.

No stars brighter than the tip of the RGB are present in the data. The lack of such super-luminous stars supports the hypothesis that GCs in M31 have ages similar to those of the Galactic GCs. Spectral line blanketing in cool giants can cause very red giants to appear fainter than the bluer, less evolved, RGB stars. This can result in some massive evolved stars appearing to have $(V - I)$ colors considerably redder than the rest of the GC stars. Our artificial star tests suggest that we are able to detect any stars above the HB so we are confident that we have not missed any super-luminous AGB stars in the outer regions of G302. However, since these stars, being more evolved, will have slightly more massive progenitors than the rest of the RGB and AGB stars, it is possible that mass segregation will have concentrated them in the inner $r = 2''.5$ of the GC making them undetectable with our data. To date no super-luminous AGB stars have been detected in any M31 GC (e.g. see Rich et al. 1996, Fusi Pecci et al. 1996, Jablonka et al. 1997 for CMDs obtained using *HST* observations). This strongly supports the idea that M31 GCs have comparable ages to those of Galactic GCs. We wish to emphasize, however, that although we see no evidence in our data for G302 having an age that is any different from the ages of the Galactic GCs, we can not rule out the presence of super-luminous stars in the inner regions of G302.

Further evidence that G302 is an old GC with an age similar to that of the Galactic GCs comes from de Freitas Pacheco (1997). That study used integrated spectra and single-population stellar populations models to estimate the ages of twelve M31 GCs—including G302. The result was a mean age of 15 ± 2.8 Gyr for their sample of twelve M31 GCs and an age of 17.0 ± 2.9 Gyr for G302.

The weighted mean magnitude of the stars in the RR Lyrae gap is $\overline{V_{\text{RR}}} = 24.93 \pm 0.09$ (standard deviation). Using this, our derived iron abundance of $[\text{Fe}/\text{H}] = -1.85$, and

$$M_V(\text{RR}) = 0.20[\text{Fe}/\text{H}] + 0.98 \quad (1)$$

(Chaboyer et al. 1996), we get a distance modulus of $\mu_0 = 24.32 \pm 0.09$ for G302.

In order to identify the outer limiting radius of G302, and to search for any radial dependence in the

morphology of the various branches of the CMD, we constructed CMDs in four annuli centered on the cluster. These CMDs are shown in Figure 5. The fiducial sequences plotted in Figure 5 are those of NGC 6397 ($[\text{Fe}/\text{H}] = -1.91$) and 47 Tuc ($[\text{Fe}/\text{H}] = -0.71$) taken from DCA. For $r \lesssim 8''$ the NGC 6397 fiducial provides a good fit to the G302 RGB. The GC appears to end at a radius somewhere between $8''$ and $11''$, in agreement with what is found by fitting MK models (see Sec. 5). Beyond $11''$ the RGB of the metal-rich halo population is clearly visible. The apparent increase in the number of blue HB stars in the inner regions of G302 is an illusion. A KS test shows that the radial distribution of blue HB stars is the same as that of the RGB stars at the 99.91% confidence level.

3.3. G312

Figure 6 shows the CMD for the GC G312. As with G302 only stars between $2''.5 \leq r \leq 10''$ are shown since star counts and the surface brightness profiles suggest that the MK tidal radius of G312 occurs at $\sim 10''$ (Holland et al. 1993, Holland 1997). Interpolating between the fiducial giant branches suggests that G312 has an iron abundance of $[\text{Fe}/\text{H}] = -0.56 \pm 0.03$, comparable to the mean iron abundance of stars in the halo of M31. This is in agreement with the spectroscopic iron abundance determined by HBK of $[\text{Fe}/\text{H}] = -0.70 \pm 0.35$. The quoted uncertainty in our iron abundance estimate is the formal uncertainty in the interpolation based on the observed width of the RGB. It does not include uncertainties in the iron abundances of the fiducial RGB sequences or uncertainties in the distance to G312. In light of this the quoted uncertainty should be considered a lower limit on the true uncertainty in our estimate of $[\text{Fe}/\text{H}]$. The small numbers of RGB stars falling under the metal-poor fiducial sequences are consistent with the expected degree of contamination (see Sec. 3.1) from disk and metal-poor halo stars in M31 (see Sec. 3.2 of HFR for details on the metallicity distribution of halo stars in M31).

The HB of G312 is a red clump located slightly to the blue of the RGB. No HB stars bluer than $(V - I)_0 = 0.6$ are present so it is not possible to determine the magnitude of the HB in the RR Lyrae gap. Therefore we estimated \overline{V}_{RR} , by taking the weighted mean magnitude of the red HB stars, to be $\overline{V}_{\text{HB}} = 25.09 \pm 0.09$. In order to get \overline{V}_{RR} we added a correction to \overline{V}_{HB} (see e.g. Lee et al. 1994) of $\Delta V_{\text{HB}}^{\text{rich}} = 0.08$ (see Sarajedini et al. 1995, Ajhar et al. 1996). This gives $\overline{V}_{\text{RR}} = 25.17 \pm 0.09$ for G312. Using the iron abundance we derived from the shape of the RGB the Chaboyer et al. (1996) relation (Eq. 1) gives a distance modulus of $\mu_0 = 24.30 \pm 0.09$.

Since so few halo stars are expected in the upper RGB of G312, the observed width of the RGB provides a good estimate of the true photometric uncertainties in our observations. Photometric and spectroscopic evidence strongly suggests that all stars in a single Galactic GC have the same metallicity and there is no evidence to suggest that this should be different for GCs in M31. The mean width of the RGB is $\sigma_{V-I} \sim 0.08$, consistent with what is predicted by the artificial star simulations (see Sec. 2.3). Therefore, we believe that the RGB width in Figure 6 is typical of a single-metallicity population for our WF observations. This Figure can be compared to Figures 4 and 5 of HFR to show that the large range of metallicities seen in the halo of M31 is not merely an artifact of photometric uncertainties along the halo RGB.

Figure 7 shows no radial dependence in the morphology of the G312 CMD.

3.4. The Color–Iron Abundance Relation

Figure 8 shows the CMDs for G302 and G312 after converting the calibrated magnitudes to absolute I -band magnitudes. This was done to determine the color of the RGB for each GC at $M_I = -3$, hereafter referred to as $(V - I)_{0,-3}$. DCA found a strong relationship between iron abundance and $(V - I)_{0,-3}$ for Galactic GCs with $-2.2 \leq [\text{Fe}/\text{H}] \leq -0.7$. Figure 9a shows the relationship between $(V - I)_{0,-3}$ and $[\text{Fe}/\text{H}]_{\text{S}}$ for G302 and G312 and several other M31 GCs with published CMDs. We have adjusted the published data to the distance modulus used in this paper ($\mu_0 = 24.3$). The $[\text{Fe}/\text{H}]_{\text{S}}$ values are the spectroscopically determined iron abundances of HBK, so the $(V - I)_{0,-3}$ color and iron abundance are determined completely independently of each other for each GC. Color, iron abundance, and reddening data for each GC is listed in Table 10 along with the source of the CMD; the projected distance of each GC from the center of M31; and Y , the projected distance of each GC from the major axis of M31 with positive Y being on the northwest side of the major axis of M31.

Since several of the M31 GCs in Figure 9a have iron abundances at least as high as that of 47 Tuc we extended the DCA relationship to higher iron abundances. Extending this relationship to GCs more metal-rich than 47 Tuc ($[\text{Fe}/\text{H}] = -0.71$) is somewhat difficult since the RGB in the $((V - I)_0, M_I)$ plane becomes asymptotically flat as the iron abundance increases. This makes it difficult to define $(V - I)_{0,-3}$ since, as $[\text{Fe}/\text{H}]$ approaches the Solar value, this point occurs in the horizontal portion of the RGB. In order to extend the DCA relationship to higher iron abundances we determined $(V - I)_{0,-3}$ for the metal-rich Galactic GC NGC 6553 using the $(I, (V - I))$ CMD of Ortolani et al. (1990). We assumed a distance modulus of $\mu_0 = 13.35$ (Guarnieri et al. 1995), a reddening of $E_{B-V} = 0.78$ (Bico & Alloin 1986), and an iron abundance of $[\text{Fe}/\text{H}] = -0.29$ (Zinn & West 1984). Using this data we found $(V - I)_{0,-3} = 2.4 \pm 0.2$ for NGC 6553. This point lies just below the region where the RGB becomes horizontal so there is a significant uncertainty in the value of $(V - I)_{0,-3}$ for NGC 6553 solely due to the width of the RGB in $(V - I)_0$ at $M_I = -3$. We extrapolated the DCA relation to $[\text{Fe}/\text{H}] = -0.29$ simply by connecting the $[\text{Fe}/\text{H}] = -0.71$ end of the DCA relation to the location of NGC 6552. The resulting relation is

$$[\text{Fe}/\text{H}] = -15.16 + 17.0(V - I)_{0,-3} - 4.9(V - I)_{0,-3}^2 \quad (2)$$

for $-2.2 \leq [\text{Fe}/\text{H}] \leq -0.7$ (from DCA) and

$$[\text{Fe}/\text{H}] = -1.36 + 0.44(V - I)_{0,-3} \quad (3)$$

for $-0.7 \leq [\text{Fe}/\text{H}] \leq -0.29$ (our extension). We wish to stress that our extension to high iron abundances is an estimate and is intended only to provide a reasonable estimate of what happens to the DCA relation at high iron abundances.

If the spectroscopic iron abundances are adopted then nine of the twelve M31 GCs are redder than predicted by the extended DCA relation. This discrepancy is present at all iron abundances but is most noticeable for the metal-rich GCs. The individual uncertainties in $[\text{Fe}/\text{H}]_{\text{S}}$ for all the GCs except G1 and G327 are large enough to account for the difference between their locations in Figure 9a and the predictions of the extended DCA relation. A recent paper by de Freitas Pacheco (1997) gives iron abundances for twelve GCs in the M31 system. Most of their iron abundances are higher than the HBK values by ~ 0.2 dex. An examination of the CMDs for each GC shows that several GCs have RGBs that are significantly redder and flatter than would be expected from their spectroscopic iron abundances. This is particularly

noticeable for the more metal-rich GCs. To test whether errors in the spectroscopically determined iron abundances are sufficient to account for the discrepancies between the GCs and the extended DCA relation in Figure 9a, we replotted the GCs using iron abundances determined from the shapes of the RGBs. This data is shown in Figure 9b. All GCs now fall within their uncertainties of the extended DCA relationship with the exception of G108, which has a $(V - I)_{0,-3}$ value nearly $3\text{-}\sigma$ redder than its predicted value. Alternately, the iron abundance Ajhar et al. (1996) derived from G108’s CMD could be in error. However, their Figure 20 shows the upper portion RGB of G108 to be not quite as flat than that of 47 Tuc, indicating that G108 has slightly less iron than 47 Tuc does. It would be difficult, using their data, to fit a fiducial to the G108 RGB that is flatter (and thus more iron rich) than the 47 Tuc fiducial. Therefore, we believe that the estimated iron abundance of G108 is correct.

One possible explanation for the red color of G108 is that the H I in M31 extends ~ 15 kpc beyond the outer edge of the optical disk, which is past the location of G108. Cuillandre et al. (1997) found dust beyond the optical limit of the M31 disk which correlates with the distribution of H I beyond the disk. Since G108 is located within the extended disk of H I around M31 it is possible that G108’s $(V - I)_{0,-3}$ color may be due to internal reddening in the extended disk of M31. Using the H I maps of Emerson (1974), and the relationships between H I column density and reddening given in Cuillandre et al. (1997), we find an excess reddening of $E_{V-I} = 0.14 \pm 0.02$. However, an examination of the CMD for G108 (Figure 20 of Ajhar et al. 1996) suggests the internal reddening from M31 does not exceed $E_{V-I} \sim 0.05$. This discrepancy may be due to the patchy nature of the H I distribution in the outer regions of M31’s extended disk. Brinks & Bajaja (1986) found many small regions in the H I distribution in M31 where the H I column densities were significantly less than the surroundings. These holes were typically a few arcminutes in diameter, smaller than the beam-size used to construct the Emerson (1974) H I maps. It is possible that G108 (which has an angular diameter of $\sim 0'.4$) is located in a hole in the H I distribution that is smaller than the resolution of the H I maps. If this is the case, the Emerson (1974) H I maps will lead to our overestimating the reddening toward G108 and our estimate of the excess reddening towards G108 would not be inconsistent with the published CMD for that GC.

4. Luminosity Functions

The raw, $n(V)$, and completeness-corrected, $\phi(V)$, V -band stellar LFs for G302 and G312 are presented in Table 11. The raw LFs include all stars within $2''.5 \leq r < 12''.5$ of the center of each GC. The background LF for each GC was obtained by taking the LF for the M31 halo near each GC (from HFR) and scaling them to the area covered by each GC. The scaled background LF was subtracted from the raw LF before the effects of incompleteness were considered. Subtracting the raw background LF assumes that the completeness corrections in the WF2 and WF4 fields are the same as in the WF3 fields. An examination of Figure 10 shows that the completeness corrections are small for stars with $V \lesssim 25$. Therefore the raw background luminosity function instead of the completeness-corrected background luminosity function will not alter the results. The raw and completeness-corrected LFs are related by $n(V) = \mathbf{P}\phi(V)$ where \mathbf{P} is the finding-probability matrix. \mathbf{P} describes the probability of a star with a true magnitude of V_{in} being recovered with a magnitude of V_{rec} .

Our artificial star tests suggest that completeness corrections need to be applied to the raw GC and background LFs. These corrections are small for $V \lesssim 25$, but the artificial star tests suggest that bin-jumping becomes significant at approximately the level of the HB and needs to be compensated for in order to accurately reconstruct the LF.

Given \mathbf{P} there is no ideal method for reconstructing a stellar LF from incomplete star counts. For a review of the problem see Fahlman (1993). Ideally the true LF, $\phi(V)$, can be obtained from the observed LF, $n(V)$, using $\phi(V) = \mathbf{P}^{-1}n(V)$ as described in Drukier et al. (1988) and Mighell (1990). Unfortunately, many faint artificial stars are lost in the noise and thus not recovered at all. This results in some artificial stars bin-jumping off the faint end of the finding-probability matrix so there is insufficient information to reliably invert \mathbf{P} . An alternative to computing \mathbf{P}^{-1} is to use a model LF, $\phi'(V)$, and solve the forward equation $n'(V) = \mathbf{P}\phi'(V)$. The estimated LF can then be adjusted until $\Delta n \equiv n - n'$ is minimized. This approach will not accurately reconstruct the faint end of the LF since \mathbf{P} does not contain sufficient information at faint magnitudes, due to bin-jumping by faint stars, to do this. However, unlike the inversion method, it will work if \mathbf{P} is nearly singular and thus allows us to estimate the completeness-corrected LF in the face of incomplete information. The drawbacks to the forward approach are that there is no obvious way to compute the uncertainties in the resulting LF and that some *a priori* information is needed about the true LF. This forward method will give different results depending on the initial guess at $\phi(V)$ and the scheme used to adjust ϕ' during the iteration. We found that, for our data, the LF is not dependent on the initial guess at the form of the LF when $V \lesssim 25$ (approximately the level of the HB). We adjusted $\phi'(V)$ using $\phi'_i(V) = \phi'_{i-1}(V) + \Delta n(V)$ and iterated $n'(V) = \mathbf{P}\phi'(V)$ until Δn was minimized.

Figure 10 shows the observed and completeness-corrected, background-subtracted LFs for G302 and G312. These LFs are reliable for $V \lesssim 25$. In Figure 11a we compare the cumulative LF for G302 with that of the metal-poor ($[\text{Fe}/\text{H}] = -1.65$) Galactic GC M13 (Simoda & Kimura 1968). In Figure 11b we compare the cumulative GC for G312 to a theoretical LF for an old ($t_0 = 14$ Gyr) GC with $[\text{Fe}/\text{H}] = -0.47$ and $[\text{O}/\text{Fe}] = +0.23$ from Bergbusch & Vandenberg (1992). Stellar evolution models do not show any relationship between the slope of the LF of the upper RGB and either the iron abundance or the age of the stars (Bergbusch & Vandenberg 1992) so Figure 11 can not be used to determine the ages or the iron abundances of G302 or G312. There is a general agreement between the shape of the G312 LF and the shape of the theoretical metal-rich LF, as well as between the shape of the G302 LF and the metal-poor comparison LF, which suggests that our star counts are reasonably complete down to the level of the HB ($V \simeq 25$).

5. Structure

5.1. Michie–King Models

We determined the tidal radii by fitting MK models to the background-subtracted surface brightness profiles of each GC. The unresolved background light was measured by masking out a circle of radius 300 pixels ($\sim 3r_t$) centered on the GC and fitting a plane to the remaining area on the WF3 CCD. We found that subtracting a constant sky level resulted in residual variations of $\lesssim 1\%$ across the WF3 CCD for both the G302 and the G312 fields. We found no evidence for intensity or color gradients in the unresolved background light.

Surface brightness profiles for each GC were obtained using the IRAF² implementation of the STSDAS task ELLIPSE. This task uses Jedrzejewski’s (1987) isophote-fitting algorithm to fit elliptical isophotes to the observed isophotes on the background-subtracted images. This algorithm determines the centers,

²Image Reduction and Analysis Facility (IRAF), a software system distributed by the National Optical Astronomy Observatories (NOAO).

ellipticities, orientations, and intensities for a series of ellipses logarithmically spaced between $\sim 0''.1$ (~ 1 pixel) and $\sim 20''.0$ (~ 200 pixels). The spacing between successive ellipses varies from significantly less than the size of the WF3 seeing disc (FWHM $\sim 0''.2$) near the center of each GC to ~ 10 times the size of the seeing disc beyond the tidal radius of the GC. The properties of the ellipses are not independent of each other for radii of less than approximately eight times the size of the seeing disc (e.g. Schweizer 1979). Since the spacing between ellipses is logarithmic the degree of correlation will vary with the distance from the center of the GC. There is an additional correlation caused by the overlap in the subsets of pixels being used to compute successive best-fitting ellipses. In light of these effects the computed uncertainties in the surface brightnesses, ellipticities, and orientations of the individual fitted ellipses should be treated as guides to the reliability of the individual values relative to the values for the other fitted ellipses for that GC and *not* taken as statistically rigorous estimates. In the inner regions of each GC ($r \lesssim 1''.0$) the large gradient in surface brightness, and the small number of pixels, make the fitted ellipses less reliable than those fit further out. Finally, we extracted the one-dimensional surface brightness profile for each GC along the effective radius axis of each GC.³

We used CERN’s MINUIT function minimization package to fit single-mass one-dimensional seeing-convolved MK models to the surface brightness profiles for each GC. The fitting was done by simultaneously adjusting all the free parameters until the χ^2_ν statistic between the model and the weighted surface brightness profile was minimized. After some experimentation we adopted a weighting scheme of $w_i = (1/\sigma_i)^2$ where σ_i is the RMS scatter in the isophotal intensity about the i^{th} fitted isophotal ellipse. We tested this weighting scheme by fitting MK models to a series of surface brightness profiles created by drawing points from a MK distribution and found good agreement between the input and the fitted models. The exact form of the weighting did not significantly affect the values of the best-fitting model parameters provided that the weights assigned to each data point were reasonably indicative of the reliability of each point.

Each MK model was convolved with the PSF for the WF3 CCD at the center of the GC. We determined the central potential, W_0 , King core radius, r_c , tidal radius, r_t , concentration, $c \equiv r_t/r_c$, anisotropy radius, r_a , and half-mass radius, r_h , for G302 and G312 in the V- and I-bands. Table 12 gives the parameters of the best-fitting MK models for each GC. The V- and I-band surface brightness profiles, along with the best-fitting MK models, are shown in Figures 12 and 13. The profiles for both GCs are well fit by isotropic MK models out to $\sim 5''$. Beyond this distance from the center of the GC there is excess light over what is predicted by isotropic ($r_a = +\infty$) MK models. In order to test if the excess light is due to velocity anisotropy in the GCs we fit anisotropic MK models to each GC. The results are listed in Table 12. In all cases the anisotropic models yield slightly larger χ^2_ν values than the corresponding isotropic models, suggesting that the isotropic models are formally better fits to the data than are the anisotropic models. Furthermore, the best-fitting anisotropy radii are greater than the fitted tidal radii for each GC, which is physically meaningless. Therefore, we conclude that the overabundance of light at large radii is not due to velocity anisotropy. This supports the hypothesis that these GCs are surrounded by extended halos of tidally stripped stars.

MINUIT returns formal uncertainties of ~ 5 to 10% on the MK parameters. However, MINUIT was generally unable to compute a fully accurate covariance matrix for the fitted parameters so MINUIT’s uncertainty estimates are not reliable. We estimated the uncertainties in our fits by generating a series of

³The effective radius, r_{eff} , of an ellipse with semi-major and semi-minor axes a and b respectively is defined by $\pi r_{\text{eff}}^2 \equiv \pi ab$. The effective radius axis is either of the two axes along which the perimeter of the ellipse intersects the perimeter of a circle with radius r_{eff} .

artificial GCs and fitting seeing-convolved MK models to them in exactly the same way that we did to our data. We found that MINUIT tended to underestimate the uncertainties in our fits by a factor of between 1.5 and 2. This suggests the true $1\text{-}\sigma$ uncertainties in the parameters are between ~ 10 and 15% of the best-fit values of the parameters.

5.2. Color Gradients

The mean color for $r_{\text{eff}} \leq 2''.5$ for G312 is $\langle(V - I)_0\rangle = 1.07$ while for G302 $\langle(V - I)_0\rangle = 0.83$. These colors are consistent with G302 having a metal-poor stellar population and G312 having a metal-rich stellar population.

Figure 14 shows the dereddened $(V - I)_0$ color profiles of G302 and G312. These profiles were obtained by subtracting the isophotal surface brightnesses in V and I then dereddening the resulting profiles. The error bars represent the $1\text{-}\sigma$ standard error in the color. The inner portion of the G302 profile is truncated at $r_{\text{eff}} \sim 0''.1$ ($= 1$ pixel) since the innermost pixels ($r \leq 1$ pixel) of our images of G302 were slightly saturated. Individual stars can be resolved to within $r_{\text{eff}} \simeq 2''.5$ of the center of the GC and the isophotes become less certain when the light becomes resolved into individual stars. Artificial star tests suggest that the large scatter in the color profiles in the outer regions of G302 and G312 represent stochastic star placement within the GCs, not intrinsic color gradients. In the inner $2''.5$ the color gradients are $d(V - I)_0/dr_{\text{eff}} = -0.028 \pm 0.007$ for G302 and $d(V - I)_0/dr_{\text{eff}} = -0.090 \pm 0.007$ for G312. To determine if these color gradients are due to chance we performed 10,000 bootstrap resamplings of the color data for each GC and computed the color gradients for each resampled data set. This analysis gave a 2.1255% probability that the observed color gradient (for $r_{\text{eff}} \leq 2''.5$) in G302 is due to chance and a 0.0005% probability that the observed color gradient (for $r_{\text{eff}} \leq 2''.5$) in G312 is due to chance.

5.3. Ellipticities

Figures 15 and 16 show the ellipticity and orientation profiles for G302 and G312 respectively. The error bars in Figures 15 and 16 should be treated as guides to the reliability of the individual measurements and *not* taken as statistically rigorous estimates of the uncertainties in each point. In order to estimate the overall projected ellipticity of each GC we determined the weighted mean ellipticities, $\bar{\epsilon}$ and position angles, $\bar{\theta}_0$ (in degrees east of north on the sky) using the values for the individual isophotes between $r_{\text{eff}} = 1''$ and $r_{\text{eff}} = 10''$. The results are presented in Table 13. The uncertainties are standard errors in the mean and N is the number of isophotes used to compute $\bar{\epsilon}$ and $\bar{\theta}_0$.

The projected major axis of G302 points approximately towards the center of M31. The ellipticity of each GC is the same in the I -band as it is in the V -band but the projected major axis of G302 in the V -band is located $16^\circ \pm 3^\circ$ west of the projected major axis in the I -band. This shift in orientation between the two colors is visible at all radii in G302 and is likely due to a small number of giant stars dominating the light from the GC. Our data show that the projected major axis of G302 in the V -band is oriented 20° farther west from the V -band orientation obtained by Lupton (1989) ($\theta_0 = 0^\circ 0' \pm 0^\circ 6'$), but that Lupton's orientation is only 4° east of our I -band orientation. This supports the idea that the difference between the I - and V -band orientations that we observed is due to the different numbers of resolved stars in the different bands and data sets. Our ellipticity ($\epsilon = 0.195 \pm 0.012$) is somewhat higher than that found by Lupton (1989) ($\epsilon = 0.15 \pm 0.02$). Figure 15 shows an apparent decrease in the ellipticity of G302 between $r_{\text{eff}} \sim 1''$

and $r_{\text{eff}} \sim 10''$. The slope of $\epsilon(r_{\text{eff}}) = mr_{\text{eff}} + b$ is $m = -0.0381 \pm 0.0383$. In order to determine if this slope represents a real decrease in ellipticity with radius we performed 10,000 bootstrap resamplings of the ellipticity data between $1'' \leq r_{\text{eff}} \leq 10''$ and computed the slope for each set of bootstrapped ellipticities. We found that there was a 22.34% chance of observing a slope at least as great as the slope seen in the actual data simply by chance. Therefore, we conclude that there is no evidence for a change in ellipticity with radius between $r_{\text{eff}} = 1''$ and $r_{\text{eff}} = 10''$ in G302. It is not possible to say if the apparent increase in ellipticity between $r_{\text{eff}} \simeq 0''.3$ and $r_{\text{eff}} \simeq 1''.0$ is real or due to the presence of a small number of unresolved bright stars located within a few core radii of the center of G302. Since the stellar FWHM is $\sim 0''.2$, the chance location of a single unresolved bright star within $0''.3$ of the center of G302 along the projected minor axis of the GC could reduce the ellipticity of the fitted isophotes.

G312 has a projected ellipticity of $\bar{\epsilon} = 0.065$ but there is considerably more scatter in the fitted position angles (the standard deviation is $\sigma \sim 27^\circ$) than in the G302 position angles ($\sigma \sim 10^\circ$). This suggests that the observed projected ellipticity of G312 is primarily due to the stochastic placement of stars within G312, variations in the stellar background of the M31 halo, and the intrinsic precision of the ELLIPSE algorithm. Running the ELLIPSE task on a series of circular artificial MK GC models which were convolved with the WF3 PSF suggests that seeing alone can produce ellipticities of between 0.01 and 0.02 at radii of between approximately $0''.5$ and $2''$. This agrees with the fluctuations in ellipticity seen in Figure 16 at these radii. While seeing has very little effect on the observed ellipticity beyond $r_{\text{eff}} \sim 2''$, artificial star tests indicate that stochastic star placement can introduce an uncertainty in the ellipticity of between ± 0.01 and ± 0.05 . In light of this we believe there is no evidence for G312 being elliptical in the plane of the sky. It is, however, possible that G312 is elongated along the line of sight.

6. Extended Stellar Halos

GAF have observed an excess of resolved and unresolved stars beyond the formal MK tidal radii of several GCs in M31, as would be expected if the stars which evaporated from these GCs remained in extended halos around those GCs. Another test for extended halos of unbound stars is to identify an asymmetrical overdensity of stars in two dimensions beyond the formal tidal radius. This has been done for some Galactic globular clusters (see Grillmair et al. 1995) using multiple Schmidt photographic plates for each GC. However, it has not been attempted for the M31 GCs, where the GC, and the background, can be imaged on a single CCD. This eliminates possible systematic effects arising from comparing star counts across multiple fields.

To search for extended halos around G302 and G312 we looked at the two-dimensional distribution of stars beyond the tidal radii of each GC. The total background stellar densities around each GC were small ($\Sigma_{\text{bkgd}} = 0.6191 \pm 0.0099$ stars/ \square'' for G302 and $\Sigma_{\text{bkgd}} = 0.1688 \pm 0.0052$ stars/ \square'' for G312). We rebinned the stellar positions into “super-pixels” so there were enough stars in each bin to ensure that the Poisson fluctuations in a bin would be small compared to the total number of stars in that bin. In order to compute the optimum binning size we assumed that all the stars on the WF3 CCD were part of the GC and that the GC could be approximated by a Gaussian distribution of stars. It can be shown (Heald 1984) that for any Gaussian distribution the bin size, δx , which maximizes the signal-to-noise in each bin, is given by $\delta x \sim (20/N)^{1/5} \sigma$ where σ is the standard deviation of the Gaussian and N is the size of the sample. This technique provides a balance between the need to keep the bin sizes small compared to the width of the Gaussian, and the need to have a large number of data-points in each bin to reduce Poisson noise in the bin. Since we are searching for overdensities of stars beyond the MK tidal radii of the GCs the

assumption that a GC can be approximated by a Gaussian will result in an underestimate of the bin size needed to maximize the signal-to-noise. We found that bin sizes of 32 pixels ($\simeq 3''.2$), approximately two to three times the computed optimal size for Gaussians, provided the best signal-to-noise for our data. We smoothed the resulting binned data by convolving it with a unit Gaussian with a dispersion equal to the bin size ($\sigma = 3''.2$). The resulting stellar number density distribution for G302 is shown in Figure 17 and the stellar number density distribution for G312 is shown in Figure 18.

Figure 17 shows an asymmetric overdensity of stars around G302 extending to at least twice the MK tidal radius. The coherence of the isodensity contours which lie beyond the tidal radius, but inside the background contour, suggests that the observed overdensities are not an artifact of the binning, smoothing, or contouring processes. The surface brightness profile of G302 (see Figure 12) light beyond the tidal radius ($r_t \sim 10''$) of the GC is in agreement with the asymmetric halo of stars seen in Figure 17. The surface brightness profile of G312, however, is consistent with there being no light beyond the tidal radius ($r_t \sim 10''$). This is reflected in the lack of an extended halo of stars in Figure 18. The fact that an overdensity of stars is seen beyond the tidal radius of G302, but not beyond the tidal radius of G312, suggests that the overdensity is real and not an artifact of the analysis.

In order to determine if the observed halo surrounding G302 is real we applied our contouring procedure to the star counts from the WF2 and WF4 images in the G302 and G312 fields. Figure 19 shows that no structures of comparable size to the halo around G302 are seen in any of the four background fields. To test whether a random distribution of stars could give rise to coherent structures which could be mistaken for an extended halo we constructed a series of random star fields with number densities comparable to those found in the G302 and G312 background fields. None of these artificial star fields showed evidence for coherent sub-structure. We also used MK surface density profiles to place artificial stars onto randomly generated star fields to see if the presence of a GC would bias our binning/smoothing/contouring process in favor of finding structure beyond the tidal radius when none was really present. None of these Monte-Carlo images showed any evidence for extended halos.

In order to quantify the orientation of the halo around G302 we computed the second moment of the distribution of stars beyond the fitted tidal radius. Only stars with $10'' \leq r \leq 35''$ from the center of the GC were used to ensure that neither the GC or the edges of the CCD biased our sample. We computed the statistic $\zeta_2 = \sqrt{\frac{1}{N} \sum_{i=1}^N y_i^2}$ where N is the number of stars beyond the tidal radius and y_i is the distance from the i^{th} star to an arbitrary axis of symmetry for the GC. This statistic corresponds to the root-mean-square distance between the stars and the axis of symmetry so the value of ζ_2 will be at its minimum when the assumed axis of symmetry coincides with the true major axis of the distribution. The ζ_2 values for G302 and G312, assuming a range of angles of symmetry, are shown in Figure 20. A second statistic, $\eta \equiv \zeta_{2,\text{max}} - \zeta_{2,\text{min}}$, gives a measure of the degree of symmetry in the distribution of stars about the center of the GC. The value of η for a distribution depends on the shape of the distribution and the number of stars present. For a given distribution, the greater the value of η measured the greater the deviation from a circular distribution of stars. For a perfectly circular distribution, ζ_2 would be the same for all angles resulting in $\eta = 0$. In order to determine the probability of getting the observed value of η by chance from a uniform circular halo of stars around a GC we generated 10,000 sets of stellar coordinates and measured η for each set. The stellar coordinates were randomly drawn from a uniform distribution of stars with the same size and number density as the field around the GC. This data formed the cumulative probability distributions shown in Figure 21. Since the stellar number density in the G302 field is different from the stellar number density in the G312 field we computed separate probability distributions for the G302 field and the G312 field.

For G302 this analysis yields $\eta = 7.4826$, which occurs at a position angle for the major axis of the extended halo of 83° ($= -97^\circ$) east of north. The cumulative probability distribution for η in the G302 fields (see Figure 21a) shows that there is only a 1.84% chance of obtaining a value of $\eta \geq 7.4826$ from a uniform distribution of stars. In contrast, the WF2 and WF4 fields near G302 yielded η values of 3.5530 and 4.6618 corresponding to 38.47% and 20.62% chances respectively of occurring by chance. The orientation of the extended halo around G302 is 10° to the west of the projected major axis of G302 as observed in the V-band and 26° west of the projected major axis for the GC as observed in the *I*-band. In light of our inability to find coherent overdensities in any of the background images or simulated images, the results of our moment analysis, and the observed overdensity of stars beyond the tidal radius of the best-fitting MK model, we believe that the extended asymmetric halo around G302 seen in Figure 17 is a real feature of G302.

Since the probability of observing a given value of η by chance depends on the number density of stars on the image we performed a separate series of 10,000 Monte-Carlo simulations for the G312 data (see Figure 21b). The resulting probability distribution indicated that the observed value of $\eta \geq 12.9960$ for the stars beyond the tidal radius G312 in the WF3 field had a 9.96% chance of occurring in a randomly distributed set of stars. The WF2 and WF4 fields around G312 have η values of 9.6342 and 9.1801 respectively, corresponding to 27.65% and 30.73% probabilities of occurring at random. This, and the lack of a significant excess of stars beyond the tidal radius of the best-fitting MK models, leads us to believe that G312 does not exhibit any evidence for having an extended halo of stars. We are not, however, able to rule out the possibility that such a halo does exist and is aligned along the line of sight.

7. Mass Loss and the Orbit of G302

7.1. Mass Loss from G302

Figures 12 and 17 show that there is an excess of light and stars beyond the tidal radius of the best-fitting MK model for G302. By computing the amount of mass beyond the tidal radius we can estimate the mass-loss rate for G302. We converted our V-band surface brightness profile for G302 to a projected mass profile using a mean mass-to-light ratio of $\Upsilon_V \equiv \mathcal{M}/L_V = 1.9$ Solar units (from Dubath & Grillmair 1997). The total mass inside the MK tidal radius ($r_t = 10''$) was $\mathcal{M} = (8.89 \pm 0.06) \times 10^5 \mathcal{M}_\odot$. We estimated the total mass of G302, by applying the mass-to-light ratio to the total integrated V-band magnitude of G302, to be $\mathcal{M}_{\text{tot}} = (9.52 \pm 0.24) \times 10^5 \mathcal{M}_\odot$. This gives a total mass of $\mathcal{M} = (0.63 \pm 0.25) \times 10^5 \mathcal{M}_\odot$ beyond the formal tidal radius of G302. Mass-segregation within a GC can result in Υ_V increasing with radius so the total mass beyond the tidal radius that we derive here will be a lower limit on the true mass in the extended halo around G302.

If we assume an age of $t_0 = 14$ Gyr and a constant rate of mass loss for G302 then the mass-loss rate required for the observed amount of mass to escape beyond the MK tidal radius is $\dot{\mathcal{M}} = 4500 \pm 1800 \mathcal{M}_\odot/\text{Gyr}$. The relaxation time at the half-mass radius for a GC is given by (Spitzer 1987)

$$t_{r,h} = 8.933 \times 10^5 (\text{yr}) \frac{\mathcal{M}_{\text{cl}}^{1/2} r_h^{3/2}}{\langle \mathcal{M}_\star \rangle \ln(0.4 N_\star)}, \quad (4)$$

where \mathcal{M}_{cl} is the total mass of the GC in Solar masses, r_h is the half-mass radius of the GC in pc, $\langle \mathcal{M}_\star \rangle$ is the mean stellar mass in the GC in Solar masses, and $N_\star \equiv \mathcal{M}_{\text{cl}}/\langle \mathcal{M}_\star \rangle$ is the estimated number of stars

in the GC. Following Djorgovski (1993) we adopted $\langle \mathcal{M}_\star \rangle = 1/3 \mathcal{M}_\odot$. The half-mass radius obtained by fitting isotropic MK models to G302 is $r_h = 1.9 \pm 0.1$ pc which gives a half-mass relaxation time of $t_{r,h} = 0.49 \pm 0.04$ Gyr. This yields a projected escape rate of $\dot{r} = (2.3 \pm 0.9) \times 10^{-3}$ per half-mass relaxation time.

Converting observed surface brightnesses to a deprojected mass profile involves solving an Abel integral which contains the radial derivative of the surface brightness distribution. Since the surface brightness data for G302 contains noise this inversion is inherently unstable. Therefore, we chose to project the theoretical escape rates of Oh & Lin (1992) into the plane of the sky before comparing them to our observed escape rate. The Oh & Lin (1992) evaporation rates for isotropic GCs with ages of $t_0 \sim 30t_{r,h}$ in the Galactic potential then become $\sim 10^{-3}$ to 10^{-2} per relaxation time. This is comparable to the escape rate inferred from our data. This result further strengthens our claim that we have detected an extended halo of unbound stars around G302.

7.2. Mass Loss from G312

Using the methods described above we find that G312 has a mass of $\mathcal{M} = (0.60 \pm 4.70) \times 10^4 \mathcal{M}_\odot$ beyond its fitted isotropic MK tidal radius ($r_t = 9''.55$). The large uncertainty in the amount of mass beyond the tidal radius is due to the large uncertainties in the surface brightness profile at large radii. Figure 18 does not show any evidence for an extended halo of stars around G312 so it is likely that the light seen beyond the fitted tidal radius in Figure 13 is due to low-level variations in the unresolved background light. Alternately, it is possible that the use of multi-mass MK models would result in a slightly larger tidal radius. If we assume that the observed excess of light in Figure 13 is due to an extended halo of stars, then the mass-loss rate required is $\dot{\mathcal{M}} = 430 \pm 3360 \mathcal{M}_\odot/\text{Gyr}$, approximately 10% of the mass-loss rate from G302. G312 has a half-mass relaxation time of $t_{r,h} = 0.29 \pm 0.02$ Gyr, so the escape rate per relaxation time is $\dot{r} = (0.38 \pm 2.95) \times 10^{-3}$. This is consistent with Oh & Lin’s (1992) theoretical values. However, the large uncertainties in our photometry near the tidal radius of G312 (and thus the large uncertainty in our observed escape rate) suggest that the observed escape rate is consistent with there being no observable mass-loss from G312.

7.3. The Orbit of G302

HBK measured a heliocentric radial velocity of -8 ± 32 km·s $^{-1}$ for G302. Correcting for Rubin & Ford’s (1970) 21 cm velocity for M31 ($v_{\text{M31}} = -297$ km·s $^{-1}$) gives G302 a radial velocity of $v = +289 \pm 32$ km·s $^{-1}$ relative to the center of M31. This is one of the largest radial velocities observed for a GC in M31, suggesting that almost all of G302’s space velocity is along the line-of-sight. This can only occur when G302 is near its perigalactic passage. Since very little of G302’s space velocity is in the plane of the sky, and G302 is near its perigalacticon, G302 must be at approximately the same distance from us as is the center of M31. This means that the distance measured on the sky between G302 and the center of M31 is the true separation; so the perigalactic distance for G302 is $\theta_p \simeq 32'.1$ corresponding to $d_p \simeq 6.77$ kpc assuming a distance modulus of $\mu_0 = 24.3$ for M31.

In order to constrain the orbit of G302 we used a three-component model for the M31 potential. The disk was modeled by a Miyamoto & Nagai (1975) potential, the bulge by a Hernquist (1990) potential, and the halo by a spherical logarithmic potential:

$$\Phi_{\text{disk}} = \frac{-G\mathcal{M}_{\text{disk}}}{\sqrt{R^2 + (a + \sqrt{z^2 + b^2})^2}}, \quad (5)$$

$$\Phi_{\text{bulge}} = \frac{-G\mathcal{M}_{\text{bulge}}}{r + c}, \quad (6)$$

$$\Phi_{\text{halo}} = V_{\text{halo}}^2 \ln(r^2 + d^2). \quad (7)$$

We adopted $\mathcal{M}_{\text{disk}} = 2.0 \times 10^{11} \mathcal{M}_{\odot}$, $\mathcal{M}_{\text{bulge}} = 6.8 \times 10^{10} \mathcal{M}_{\odot}$, $a = 7.8$ kpc, $b = 0.31$ kpc, $c = 0.84$ kpc, $d = 14.4$ kpc, and $V_{\text{halo}} = 128 \text{ km}\cdot\text{s}^{-1}$. These parameters were chosen by scaling the Galactic values to the observed mass and diameter of M31.

Using this model, and the observed radial velocity and perigalactic distance of G302, we found that the orbit of G302 has an eccentricity of $e \equiv (d_a - d_p)/(d_a + d_p) = 0.65$ where d_a is the apogalactic distance (in kpc) for G302. This value assumes that all of the space velocity of G302 is along the line-of-sight, and gives G302 an apogalactic distance of $\theta_a = 2^\circ.5$ or $d_a = 31.5$ kpc. If we allow 40% of G302's space velocity to be in the plane of the sky then the orbital parameters become $e = 0.71$ and $d_a = 37.0$. Since G302's radial velocity is faster than 95% of the radial velocities of other M31 GCs it is unlikely that more than $\sim 5\%$ of G302's space velocity is tangential to the line-of-sight. If this is the case, the orbital eccentricity for G302 is $0.65 \lesssim e \lesssim 0.66$ and the apogalactic distance is $d_a = 31.5$ kpc. The period of G302's orbit was defined to be twice the time required for the GC to move from its perigalacticon to its apogalacticon. If all of the GC's space velocity is along the line-of-sight then the orbital period is $P = 0.42$ Gyr. If 40% of the space velocity is tangential to the line-of-sight then $P = 0.52$ Gyr.

8. Implications of the *Hipparcos* Distance Scale

Since this work was completed new parallax measurements from the *Hipparcos* satellite have been published which have led to a revised estimate of the distance to M31. The new distance modulus is $\mu_0 = 24.77 \pm 0.11$ (Feast & Catchpole 1997), which corresponds to a distance of $d = 900 \pm 45$ kpc, a 25% increase over the distance that we adopted for M31. If this distance modulus is used then our results change in the following ways:

1. Adjusting the fiducial RGB sequences in Sec. 3.2 and Sec. 3.3 yields iron abundances of $[\text{Fe}/\text{H}] = -2.2$ for G302 and $[\text{Fe}/\text{H}] = -0.7$ for G312. The new G312 iron abundance is consistent with the HBK spectroscopic iron abundance but the new G302 value is $\sim 2.5\text{-}\sigma$ lower than the HBK or the de Freitas Pacheco (1997) value.
2. Chaboyer et al. (1997) have derived a new relation, $M_V(\text{RR}) = (0.23 \pm 0.04)([\text{Fe}/\text{H}] + 1.9) + (0.41 \pm 0.08)$, between $[\text{Fe}/\text{H}]$ and $M_V(\text{RR})$ which uses the *Hipparcos* parallaxes. This relation, and the iron abundances and HB magnitudes derived in Sec. 3.2 and Sec. 3.3, gives distance moduli of $\mu_0 = 24.51 \pm 0.12$ for G302 and $\mu_0 = 24.45 \pm 0.13$ for G312. These distance moduli would place G302 ~ 100 kpc in front of M31 if M31 is 900 kpc away. This is inconsistent with the HBK radial velocity of G302 and the orbital parameters determined in Sec. 7.3. The distance modulus for G312, and the Feast & Catchpole (1997) distance to M31, puts this GC ~ 125 kpc in front of M31.

3. Adopting a distance modulus of $\mu_0 = 24.77 \pm 0.11$ would result in the metal-rich GCs in Figure 9 being in better agreement with the DCA relation and our extension to it. However, the metal-poor GCs would have bluer $(V - I)_{0,-3}$ colors which would result in them falling to the left of the DCA relation. This would mean that the spectroscopic iron abundances of the metal-poor M31 GCs have been systematically overestimated. Since iron abundances are more difficult to determine in spectra of metal-rich GCs it is more likely that the $[\text{Fe}/\text{H}]$ values for the metal-rich GCs have been underestimated than the $[\text{Fe}/\text{H}]$ values for the metal-poor GCs have been underestimated.

In light of these results we find no reason to prefer the $\mu_0 = 24.77 \pm 0.11$ distance modulus over the $\mu_0 = 24.3 \pm 0.1$ value.

9. Conclusions

We have used *HST* WFPC2 photometry to construct deep ($V \simeq 27$) CMDs for two GCs in the halo of M31. Both GCs appear to have a single old population of stars similar to what is found in Galactic GCs. The shape of the RGB for G302 gives an iron abundance of $[\text{Fe}/\text{H}] = -1.85 \pm 0.12$, in agreement with the published values obtained using spectroscopy. For G312 we obtain $[\text{Fe}/\text{H}] = -0.56 \pm 0.03$, which is somewhat more metal-rich than the spectroscopic value. Neither GC shows any indication that there is a second parameter acting upon their HB morphologies.

Both GCs have MK tidal radii of $r_t \simeq 10''$, core radii of $r_c \simeq 0''.2$, central concentrations of $c \simeq 1.7$, and half-mass radii of $r_h \simeq 0''.5$. There is no evidence for velocity anisotropy in either G302 or G312. G302 has a color of $(V - I)_0 = 0.83$ while the color of G312 is $(V - I)_0 = 1.07$.

G302 has a projected ellipticity of $\epsilon = 0.195$ with the major axis oriented approximately towards the center of M31. This GC has an excess of light beyond its formal tidal radius which is not consistent with either an isotropic or an anisotropic MK model. The two-dimensional distribution of stars around G302 is consistent with the presence of an extended halo extending to two to three times the formal tidal radius from the cluster. G312, on the other hand, has an ellipticity of $\epsilon \simeq 0$. Neither the integrated light, nor the star counts, show any evidence for an extended halo. It is possible that such a tail does exist for G312, but is oriented along the line of sight.

We have estimated the projected mass-loss rate from G302 to be $\dot{M} = 4500 \pm 1800 \mathcal{M}_\odot$ per Gyr which corresponds to a projected escape rate of $\dot{r} = (2.3 \pm 0.9) \times 10^{-3}$ per half-mass relaxation time. The projected escape rate from G312 is $\dot{r} = (0.38 \pm 2.95) \times 10^{-3}$ per half-mass relaxation time. These are consistent with the escape rates predicted by Oh & Lin (1992) although the large photometric uncertainties near the tidal radius of G312 makes the escape rate for this GC much less reliable than that for G302.

This research is based on observations made with the NASA/ESA *Hubble Space Telescope* obtained at the Space Telescope Science Institute. STScI is operated by the Association of Universities for Research in Astronomy Inc. under NASA contract NAS 5-26555. Support for this research was provided by operating grants to GGF and HBR from the Natural Science and Engineering Research Council of Canada. SH would like to thank Peter Stetson for kindly making a copy of the ALLFRAME software, as well as *V*- and *I*-band PSFs for the WFC, available. We would also like to thank the anonymous referee who made several useful comments.

REFERENCES

- Ajhar, E. A., Grillmair, C. J., Lauer, T. R., Baum, W. A., Faber, S. M., Holtzman, J. A., Lynds, C. R., & O’Neil, Jr., E. J. 1996, *AJ*, 111, 1110
- Ashman, K. M., Conti, A., & Zepf, S. E. 1995, *AJ*, 110, 1164
- Baev, P. V., Spassova, N., & Staneva, A. 1997, *A&A*, 319, 45
- Battistini, P., Bònoli, F., Buonanno, R., Corsi, C. E., & Fusi Pecci, F. 1982, *A&A*, 113, 39
- Bendinelli, O., Parmeggiani, G., Zavatti, F., & Djorgovsky, S. 1990, *AJ*, 99, 774
- Bendinelli, O., Cacciari, C., Djorgovski, S., Federici, L., Ferraro, F. R., Fusi Pecci, F., Parmeggiani, G., Weir, N., & Zavatti, F. 1993, *ApJ*, 409, L17
- Bergbusch, P. A., & VandenBerg, D. A. 1992, *ApJS*, 81, 163
- Bico, E., & Alloin, D. 1986, *A&A*, 162, 21
- Brinks, E., & Bajaja, E. 1986, *A&A*, 169, 14
- Christian, C. A., & Heasley, J. N. 1991, *AJ*, 101, 848
- Cohen, J. G., & Freeman, K. C. 1991, *AJ*, 101, 483
- Couture, J., Racine, R., Harris, W. E., & Holland, S. 1995, *AJ*, 109, 2050
- Chaboyer, B., Demarque, P., & Sarajedini, A. 1996, *ApJ*, 459, 558
- Chaboyer, B., Demarque, P., Kernan, P. J., Krauss, L. M. 1997, submitted to *ApJ*
- Crampton, D., Cowley, A. P., Schade, D., & Chayer, P. 1985, *ApJ*, 288, 494
- Cuillandre, J.-C., Lequeux, J., Mellier, Y., & Allen, R. J. 1997, submitted to *A&A*
- Da Costa, G. S., & Armandroff, T. E. 1990, *AJ*, 100, 162 (DCA)
- de Freitas Pacheco, J. A. 1997, *A&A*, 319, 394
- Djorgovski, S. 1993, in *Structure and Dynamics of Globular Clusters*, ASP Conf. Ser. 50, edited by S. Djorgovski and G. Meylan (ASP, San Fransisco), p. 347
- Drukier, G. A., Fahlman, G. G., Richer, H. B., & VandenBerg, D. A. 1988, *AJ*, 95, 1415
- Dubath, P., & Grillmair, C. J. 1997, *A&A*, 321, 379
- Emerson, D. T. 1974, *MNRAS*, 169, 607
- Fahlman, G. G. 1993, in *The Globular Cluster–Galaxy Connection*, ASP Conf. Ser. 48, edited by G. H. Smith, & J. P. Brodie, (San Francisco, ASP), p. 117
- Feast, M. W., & Catchpole, R. M. 1997, *MNRAS*, 286, L1
- Fusi Pecci, F., Battistini, P., Bendinelli, O., Bònoli, F., Cacciari, C., Djorgovski, S., Federici, L., Ferraro, F. R., Parmeggiani, G., Weir, N., & Zavatti, F. 1994, *A&A*, 284, 349
- Fusi Pecci, F., Buonanno, R., Cacciari, C., Corsi, C. E., Djorgovski, S. G., Federici, L., Ferraro, F. R., Parmeggiani, G., & Rich, R., M. 1996, *AJ*, 112, 1461
- Grillmair, C. J., Freeman, K., C., Irwin, M., & Quinn, P. J. 1995, *AJ*, 109, 2553
- Grillmair, C. J., Ajhar, E. A., Faber, S. M., Baum, W. A., Holtzman, J. A., Lauer, T. R., Lynds, C. R., & O’Neil, Jr., E. J. 1996, *AJ*, 111, 2293 (GAF)

- Guarnieri, M. D., Montegriffo, P., Ortolani, S., Moneti, A., Barbuy, B., & Bica, E. 1995, *ESO Messenger*, 79, 26
- Gunn, J. E., & Griffin, R. F. 1979, *AJ*, 84, 752
- Harris, W. E. 1991, *ARA&A*, 29, 543
- Heald, M. A. 1984, *Am. J. Phys.*, 52, 254
- Heasley, J. N., Christian, C. A., Friel, E. D., & Janes, K. A. 1988, *AJ*, 96, 1312
- Hernquist, L. 1990, *ApJ*, 356, 359
- Hodge, P. 1992, *The Andromeda Galaxy*, (Kluwer, Dordrecht)
- Holland, S., Fahlman, G. G., & Richer, R. B. 1993, *BAAS*, 25, 885
- Holland, S., Fahlman, G. G., & Richer, R. B. 1996, *AJ*, 112, 1035 (HFR)
- Holland, S. 1997, PhD. Thesis, in preparation
- Holtzman, J. A., Burrows, C. J., Casertano, S., Hester, J. J., Trauger, J. T., Waterson, A. M., & Worthey, G. S., 1995, *PASP*, 107, 1065
- Huchra, J. P., Brodie, J. P., & Kent, S. M. 1991, *ApJ*, 370, 495 (HKB)
- Innanen, K. A., Harris, E. W., & Webbink, R. F. 1983, *AJ*, 88, 338
- Jablonka, P., Bridges, T., Sarajedini, A., Meylan, G., Meynet, G., & Maeder, A. 1997, *BAAS*, 28, 1364
- Jedrzejewski, R. I. 1987, *MNRAS*, 226, 747
- King, I. R. 1962, *AJ*, 67, 471
- King, I. R. 1966, *AJ*, 71, 64
- Lee, Y.-W., Demarque, P., & Zinn, R. J., *ApJ*, 423, 248
- Lupton, R. H. 1989, *AJ*, 97, 1350
- Michie, R. W. 1963, *MNRAS*, 125, 127
- Mighell, K. J. 1990, *A&AS*, 82, 207
- Miyamoto, M., & Nagai, R. 1975, *PASJ*, 27, 533
- Moffat, A. F. J. 1969, *A&A*, 3, 455
- Oh, K. S., & Lin, D. N. C. 1992, *ApJ*, 386, 519
- Ortolani, S., Barbuy, B., & Bica, E. 1990, *A&A*, 236, 362
- Okazaki, T., & Tosa, M. 1995, *MNRAS*, 274, 48
- Pritchett, C., & van den Bergh, S. 1984, *PASP*, 96, 804
- Rich, R. M., Mighell, K. J., Freedman, W. L., & Neill, J. D. 1996, *AJ*, 111, 768
- Rubin, V. C., & Ford, W. K. 1970, *ApJ*, 159, 379
- Sarajedini, A., Lee, Y.-W., & Lee, D. H., *ApJ*, 450, 712
- Sargent, W. L., Kowal, C., Hartwick, F. D. A., & van den Bergh, S. 1977, *AJ*, 82, 947
- Schweizer, F. 1979, *ApJ*, 233, 23
- Simoda, M., & Kimura, H. 1968, *ApJ*, 151, 133
- Spassova, N. M., Staneva, A. V., & Golev, V. K. 1988, in *Globular Clusters in Galaxies*, edited by J. E. Grindley, & A. G. Davis Philip, (Kluwer, Dordrecht), 569

- Spitzer, L. 1987, *Dynamical Evolution of Globular Clusters*, (Princeton, Princeton University Press)
- Stetson, P. B. 1987, *PASP*, 99, 191
- Stetson, P. B. 1994, *PASP*, 106, 250
- Stetson, P. B. 1996, private communication
- Stetson, P. B. & Harris, W. E. 1988, *AJ*, 96, 909
- West, M. J., Côté, P., Jones, C., Forman, W., & Marzke, R. O. 1995, *ApJ*, 453, L77
- van den Bergh, S. 1991, *PASP*, 103, 1053
- Zinn, R. & West, M. 1984, *ApJS*, 55, 45

Table 1. Log of the Observations.

Field	Date (1995)	Filter	Exposure (s)
G302	Nov. 5	F555W	8×500
			2×160
		F814W	7×500
			1×400
			1×160
G312	Oct. 31	F555W	8×500
			2×160
		F814W	7×500
			1×400
			1×160

Table 2. Aperture Corrections.

Field	CCD	Filter	$\langle \text{ap} - \text{PSF} \rangle$	Slope	N
G302	PC	F555W	-0.0226 ± 0.0355	0.992	12
		F814W	-0.0222 ± 0.0218	1.009	29
	WF2	F555W	$+0.0184 \pm 0.0216$	1.065	25
		F814W	$+0.0374 \pm 0.0099$	1.017	80
	WF3	F555W	-0.0124 ± 0.0101	1.003	87
		F814W	$+0.0150 \pm 0.0063$	1.018	217
	WF4	F555W	$+0.0333 \pm 0.0119$	1.011	90
		F814W	$+0.0297 \pm 0.0053$	1.005	252
G312	PC	F555W
		F814W
	WF2	F555W	-0.0344 ± 0.0144	1.008	186
		F814W	$+0.0405 \pm 0.0087$	1.034	119
	WF3	F555W	-0.0198 ± 0.0081	1.018	101
		F814W	-0.0030 ± 0.0013	1.015	125
	WF4	F555W	$+0.0513 \pm 0.0165$	1.001	85
		F814W	$+0.0333 \pm 0.0102$	1.027	89

Table 3. Stellar Photometry for G302 and the Surrounding Fields.

CCD	ID	X	Y	V	σ_V	χ_V	I	σ_I	χ_I
WF3	892	64.328	212.348	17.032	0.082	1.000	16.294	0.071	1.000
WF2	3440	466.457	631.376	17.628	0.084	0.744	16.365	0.077	0.727
WF3	2583	437.139	413.836	18.195	0.065	1.341	17.356	0.059	1.551
WF3	2606	439.952	415.701	18.454	0.063	1.462	17.642	0.064	1.830
WF3	2489	438.016	410.038	18.854	0.095	1.700	17.995	0.057	1.240
WF4	4532	300.305	699.237	19.152	0.031	0.739	17.418	0.030	0.877
WF3	2474	441.016	410.137	19.183	0.111	1.823	17.977	0.073	1.819
WF2	150	321.521	80.650	19.311	0.036	0.657	16.489	0.089	0.941
WF2	2719	310.787	523.757	19.669	0.070	1.499	18.432	0.063	1.959
WF3	2554	442.354	412.389	19.741	0.101	1.325	18.639	0.076	1.507

Table 4. Stellar Photometry for G312 and the Surrounding Fields.

CCD	ID	X	Y	V	σ_V	χ_V	I	σ_I	χ_I
WF3	503	689.043	346.030	17.369	0.050	0.827	16.723	0.025	0.758
WF2	1198	252.106	634.779	17.758	0.057	0.745	16.875	0.055	0.830
WF4	537	650.877	360.807	17.934	0.051	0.982	17.217	0.026	0.801
WF3	802	417.826	417.893	17.983	0.060	1.509	17.020	0.061	1.704
WF4	869	310.743	507.150	18.569	0.028	0.630	17.479	0.026	0.789
WF3	811	419.875	419.020	18.662	0.078	1.841	17.422	0.053	1.494
WF3	1654	229.986	766.329	18.743	0.035	0.907	18.116	0.019	0.601
WF3	412	167.937	301.246	18.896	0.034	0.877	16.521	0.030	0.756
WF3	770	415.495	417.557	19.926	0.055	1.014	18.819	0.065	1.407
WF3	1451	676.379	661.313	20.225	0.038	0.948	18.614	0.025	0.736

Table 5. Stellar Photometry for G302.

CCD	ID	X	Y	r	V	σ_V	χ_V	I	σ_I	χ_I
WF3	2583	437.139	413.836	0''230	18.195	0.065	1.341	17.356	0.059	1.551
WF3	2606	439.952	415.701	0''332	18.454	0.063	1.462	17.642	0.064	1.830
WF3	2489	438.016	410.038	0''265	18.854	0.095	1.700	17.995	0.057	1.240
WF3	2474	441.016	410.137	0''308	19.183	0.111	1.823	17.977	0.073	1.819
WF3	2554	442.354	412.389	0''332	19.741	0.101	1.325	18.639	0.076	1.507
WF3	2532	429.789	412.006	0''921	20.376	0.079	1.847	19.356	0.067	1.961
WF3	2420	440.762	402.723	0''989	20.812	0.071	1.629	19.648	0.063	1.828
WF3	2553	428.372	414.756	1''084	20.947	0.058	1.355	19.735	0.043	1.256
WF3	2460	418.943	405.789	2''108	21.148	0.027	0.679	19.992	0.029	0.922
WF3	2456	427.305	405.329	1''368	21.241	0.048	1.071	19.853	0.046	1.304

Table 6. Stellar Photometry for G312.

CCD	ID	X	Y	r	V	σ_V	χ_V	I	σ_I	χ_I
WF3	802	417.826	417.893	0''039	17.983	0.060	1.509	17.020	0.061	1.704
WF3	811	419.875	419.020	0''198	18.662	0.078	1.841	17.422	0.053	1.494
WF3	770	415.495	417.557	0''274	19.926	0.055	1.014	18.819	0.065	1.407
WF3	866	417.573	427.651	0''972	22.019	0.086	1.941	20.250	0.045	1.217
WF3	783	429.730	414.665	1''191	22.086	0.056	1.330	20.499	0.050	1.467
WF3	803	405.224	418.070	1''294	22.180	0.053	1.224	20.275	0.048	1.413
WF3	841	396.894	424.414	2''221	22.310	0.073	1.267	20.965	0.059	1.244
WF3	871	412.104	427.591	1''141	22.355	0.072	1.544	21.183	0.066	1.812
WF3	915	418.244	434.008	1''603	22.645	0.079	1.777	21.687	0.068	1.789
WF3	796	434.824	416.729	1''658	22.676	0.041	0.920	21.468	0.035	0.953

Table 7. Photometric Uncertainties.

V	G302 σ_V	G312 σ_V	I	G302 σ_I	G312 σ_I
20.25	20.25	0.031	...
20.75	20.75	0.026	0.023
21.25	21.25	0.031	0.028
21.75	0.038	...	21.75	0.036	0.033
22.25	0.037	...	22.25	0.038	0.039
22.75	0.043	0.046	22.75	0.046	0.043
23.25	0.049	0.049	23.25	0.051	0.049
23.75	0.055	0.051	23.75	0.067	0.063
24.25	0.065	0.062	24.25	0.081	0.077
24.75	0.079	0.077	24.75	0.118	0.099
25.25	0.094	0.090	25.25	0.145	0.153
25.75	0.129	0.121	25.75	0.217	0.222
26.25	0.176	0.182	26.25	0.333	0.314
26.75	0.262	0.271	26.75	0.570	0.457
27.25	0.356	0.310	27.25
27.75	27.75
28.25	28.25

Table 8. Magnitude shifts in RGB artificial star data.

V	$[V]$	$[\sigma_V]$	$[\delta_V]$	$\hat{\sigma}_V$	$[(V - I)_0]$	$[\sigma_{(V-I)_0}]$	$[\delta_{(V-I)_0}]$	$\hat{\sigma}_{(V-I)_0}$	N
22.5–23.0	22.947	0.058	−0.008	0.039	1.536	0.074	0.002	0.049	2
23.0–23.5	23.361	0.065	−0.030	0.061	1.382	0.082	−0.013	0.028	19
23.5–24.0	23.800	0.064	−0.006	0.056	1.237	0.089	−0.010	0.062	31
24.0–24.5	24.262	0.081	0.024	0.055	1.081	0.102	0.009	0.064	55
24.5–25.0	24.781	0.087	0.023	0.085	1.007	0.115	0.028	0.087	78
25.0–25.5	25.251	0.104	0.041	0.098	0.918	0.138	−0.006	0.094	110
25.5–26.0	25.752	0.128	0.043	0.176	0.890	0.177	−0.009	0.187	116
26.0–26.5	26.235	0.179	0.068	0.277	0.881	0.244	0.004	0.192	88
26.5–27.0	26.654	0.232	0.138	0.412	0.873	0.319	0.042	0.184	33
27.0–27.5	27.076	0.308	0.347	0.052	0.826	0.415	−0.011	0.169	3

Table 9. Magnitude shifts in HB artificial star data.

V	$[V]$	$[\sigma_V]$	$[\delta_V]$	$\hat{\sigma}_V$	$[(V - I)_0]$	$[\sigma_{(V-I)_0}]$	$[\delta_{(V-I)_0}]$	$\hat{\sigma}_{(V-I)_0}$	N
24.0–24.5	24.384	0.073	−0.744	0.100	0.623	0.106	0.099	0.159	12
24.5–25.0	24.911	0.086	−0.194	0.123	0.429	0.134	0.010	0.181	94
25.0–25.5	25.182	0.102	0.055	0.090	0.537	0.153	−0.020	0.136	823
25.5–26.0	25.615	0.214	0.486	0.200	0.945	0.236	0.400	0.293	12
26.0–26.5	26.054	0.246	0.890	0.000	1.569	0.274	0.856	0.000	1

Table 10. The GC Data.

Cluster	$(V - I)_{0,-3}$	$[\text{Fe}/\text{H}]_{\text{S}}$	$[\text{Fe}/\text{H}]_{\text{CMD}}$	E_{V-I}	R_{M31}	Y	Reference
G1	1.47 ± 0.06	-1.08 ± 0.09	-0.65 ± 0.10	0.10 ± 0.03	152'3	+29'1	4
G11	1.22 ± 0.04	-1.89 ± 0.17	-1.7 ± 0.20	0.10 ± 0.03	75'7	+43'6	2
G58	1.80 ± 0.05	-0.57 ± 0.15	-0.57 ± 0.15	0.14 ± 0.04	28'2	+27'3	1
G105	1.31 ± 0.02	-1.49 ± 0.17	-1.49 ± 0.17	0.08 ± 0.02	64'8	−29'9	1
G108	1.62 ± 0.05	-0.94 ± 0.27	-0.80 ± 0.10	0.15 ± 0.04	20'8	+19'7	1
G219	1.20 ± 0.02	-1.83 ± 0.22	-2.04 ± 0.22	0.08 ± 0.02	87'2	−58'8	1
G302	1.24 ± 0.04	-1.76 ± 0.18	-1.85 ± 0.12	0.10 ± 0.03	32'1	−30'4	3
G312	1.88 ± 0.07	-0.70 ± 0.35	-0.56 ± 0.03	0.10 ± 0.03	49'8	−49'7	3
G319	1.70 ± 0.17	-0.66 ± 0.22	-0.6 ± 0.90	0.10 ± 0.03	72'1	−69'0	2
G323	1.17 ± 0.04	-1.96 ± 0.29	-2.0 ± 0.20	0.10 ± 0.03	53'8	−53'8	2
G327	1.31 ± 0.06	-1.78 ± 0.11	-1.3 ± 0.30	0.10 ± 0.03	99'7	+19'9	2
G352	1.84 ± 0.06	-0.85 ± 0.33	-0.5 ± 0.10	0.10 ± 0.03	87'1	−49'6	2

References. — (1) Ajhar et al. 1996; (2) Couture et al. 1995; (3) this work; (4) Rich et al. 1996.

Table 11. V-Band Luminosity Functions for G302 and G312.

V	$n_{\text{G302}}(V)$	$\phi_{\text{G302}}(V)$	$n_{\text{G312}}(V)$	$\phi_{\text{G312}}(V)$
21.75	3	2.719	0	0.000
22.25	17	16.184	0	0.000
22.75	26	22.139	2	0.725
23.25	32	20.397	19	16.635
23.75	46	34.960	12	4.148
24.25	58	61.228	25	26.724
24.75	125	166.622	48	57.009
25.25	116	43.772	85	139.459
25.75	62	0.000	36	61.921
26.25	50	142.707	26	157.769
26.75	25	0.000	13	313.156
27.25	4	0.000	3	216.386

Table 12. Best-Fitting Michie–King Models.

Cluster	Filter	W_0	r_c	r_t	c	r_a	r_h	χ^2_ν	ν
G302	V	7.56	0''20	9''92	1.70	$+\infty$	0''52	1.827	49
		7.61	0''20	10''12	1.71	282''40	0''54	1.855	48
	I	7.65	0''20	10''49	1.73	$+\infty$	0''56	0.846	51
		7.47	0''21	9''80	1.67	20''06	0''49	0.906	48
G312	V	7.57	0''19	9''51	1.70	$+\infty$	0''53	0.839	53
		7.48	0''20	9''16	1.67	492''13	0''49	0.882	52
	I	7.46	0''21	9''64	1.67	$+\infty$	0''49	0.458	53
		7.47	0''21	9''70	1.67	381''88	0''49	0.467	52

Table 13. Ellipticities and position angles.

Cluster	Filter	$\bar{\epsilon}$	$\overline{\theta_0}$	N
G302	V	0.194 ± 0.011	$-71^\circ \pm 2^\circ$	24
	I	0.195 ± 0.012	$-87^\circ \pm 2^\circ$	24
G312	V	0.072 ± 0.015	$77^\circ \pm 5^\circ$	24
	I	0.058 ± 0.014	$77^\circ \pm 6^\circ$	24

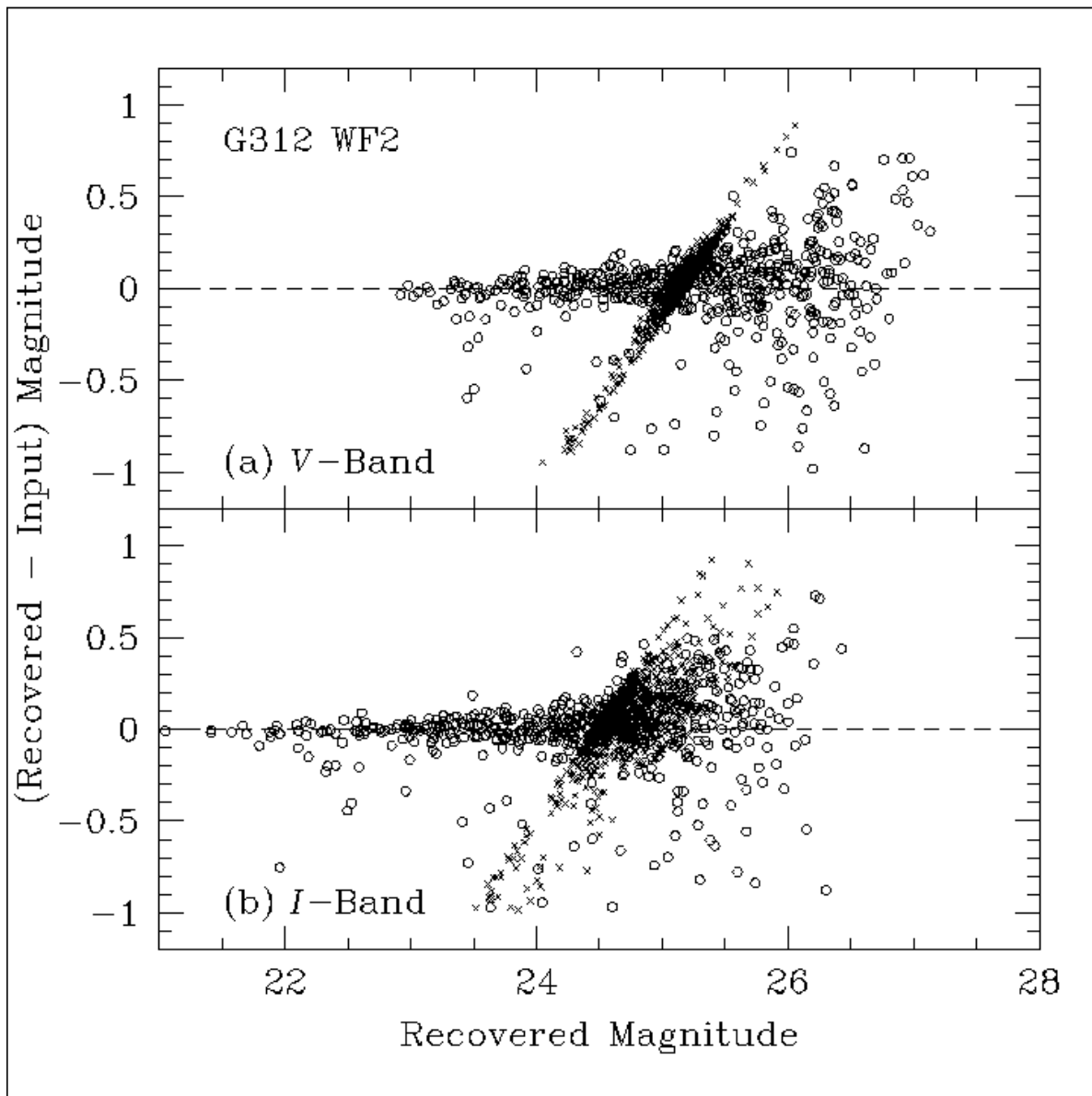


Fig. 1.— This figure shows the scatter in the recovered magnitudes of the artificial stars added to the WF2 background field $\sim 1'$ south of the GC G312. The upper (a) panel shows the observed shifts in magnitudes for the V-band photometry while the lower (b) panel shows the observed shifts in magnitude for the I-band photometry. Open circles, “o”, denote RGB stars while crosses, “x” denote HB stars. Only stars with shifts of less than 1 mag are shown. Negative magnitude shifts indicate that the star was recovered brighter than it was input. Positive shifts indicate the star was recovered fainter than it was input. KS tests show that the distributions of recovered magnitudes for the artificial RGB and HB stars are the same at the 98.892% confidence level in the V-band and are the same at the 99.999% confidence level in the I-band. The apparent excess scatter in the HB artificial stars is merely an artifact of the large number of artificial HB stars.

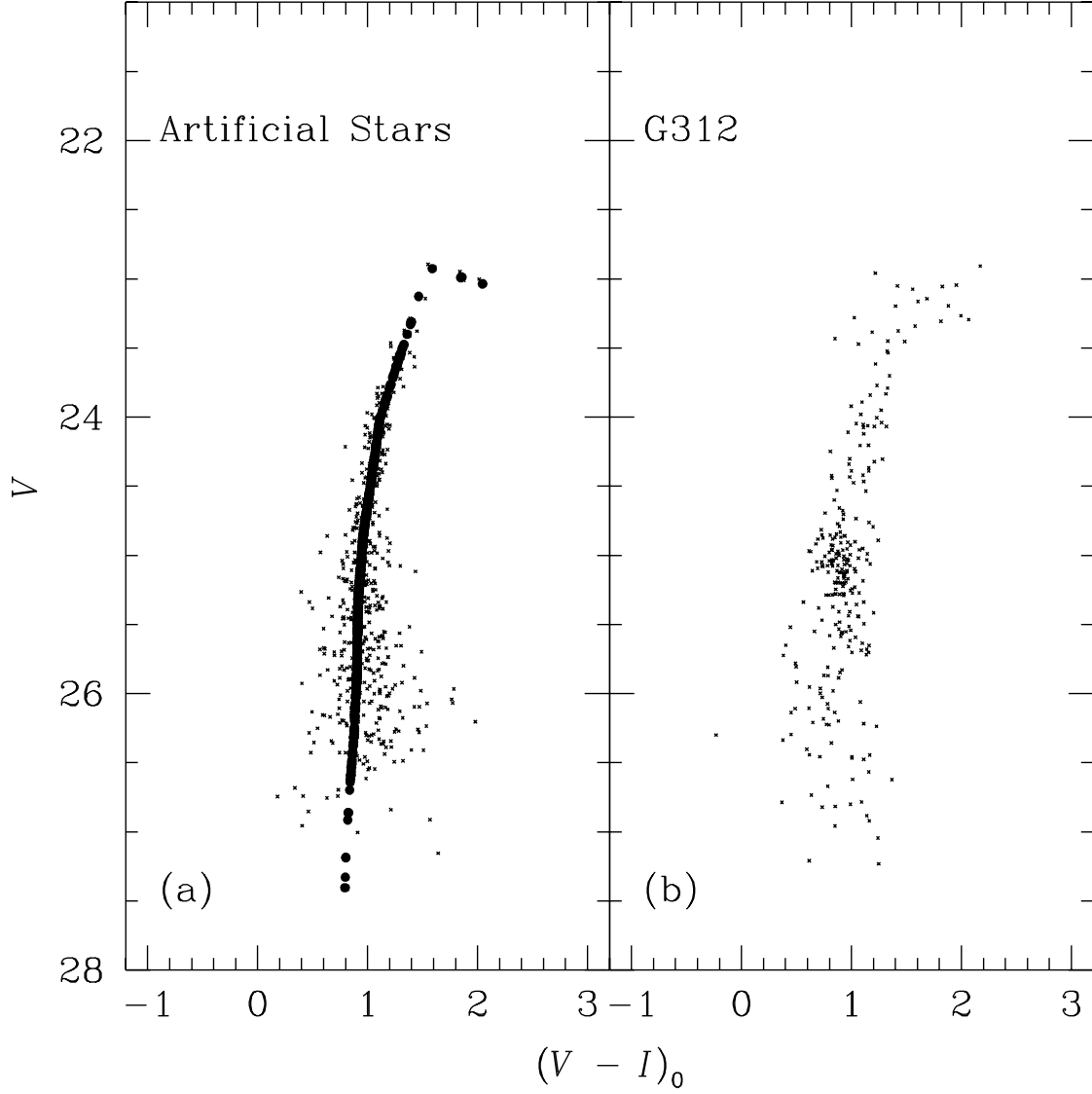


Fig. 2.— The left-hand panel (a) shows a CMD for a set of artificial stars added to the G312 WF3 field. Solid circles, “•”, represent the input colors and magnitudes while crosses, “×”, represent the recovered photometry. For clarity only RGB stars are shown in this figure. The right-hand panel (b) shows the observed CMD for RGB stars in G312. The spread in the recovered colors of the artificial stars is approximately the same as the spread in color observed in the G312 CMD, suggesting that the observed width of the RGB is due to photometric uncertainties and is not intrinsic to G312.

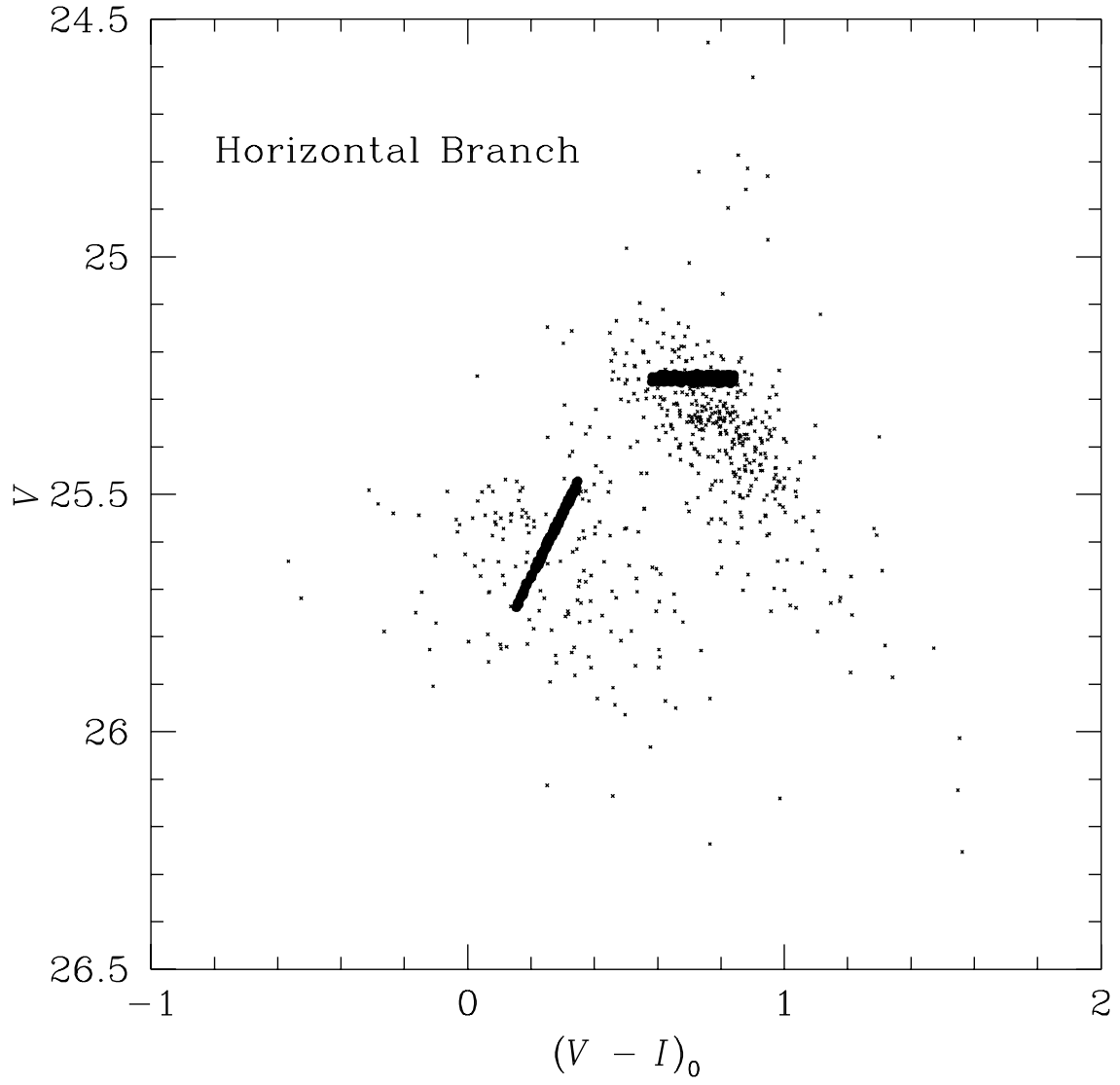


Fig. 3.— The solid circles, “•”, show the input artificial HB. The HB has been divided into distinct red and blue parts to aid in the identification of scatter from each component. Crosses, “×”, show the recovered colors and magnitudes of the artificial stars.

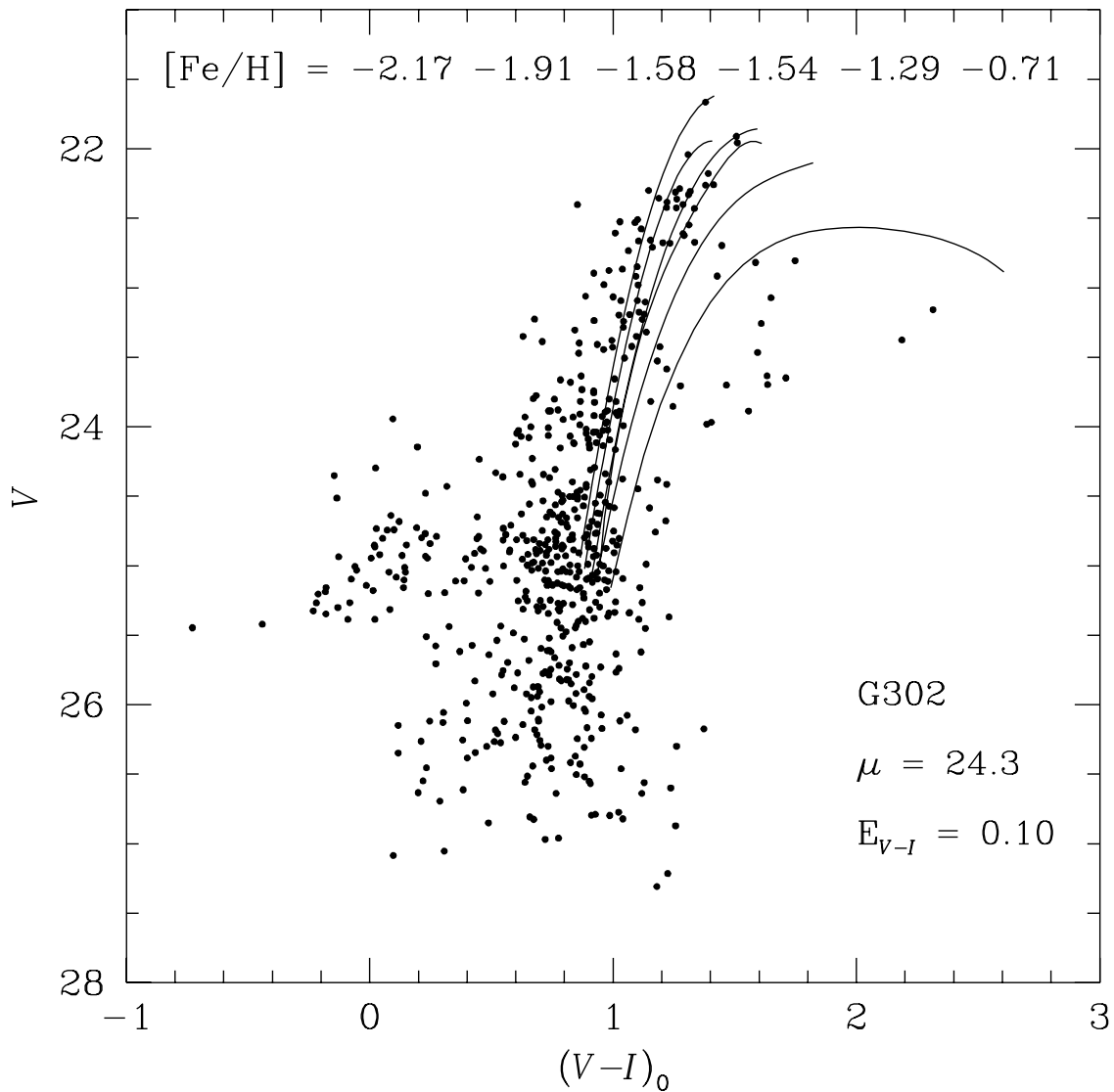


Fig. 4.— The CMD for G302. Only stars between $2''.5 \leq r \leq 10''$ are plotted to minimize contamination from stars in the halo of M31 and from unreliable photometry due to the extreme crowding in the central regions of G302. The distinct blue HB is consistent with a metal-poor stellar population. The RGB fiducial sequences are of Galactic GCs and were taken from DCA. The iron abundances for each fiducial line is printed at the top of the figure.

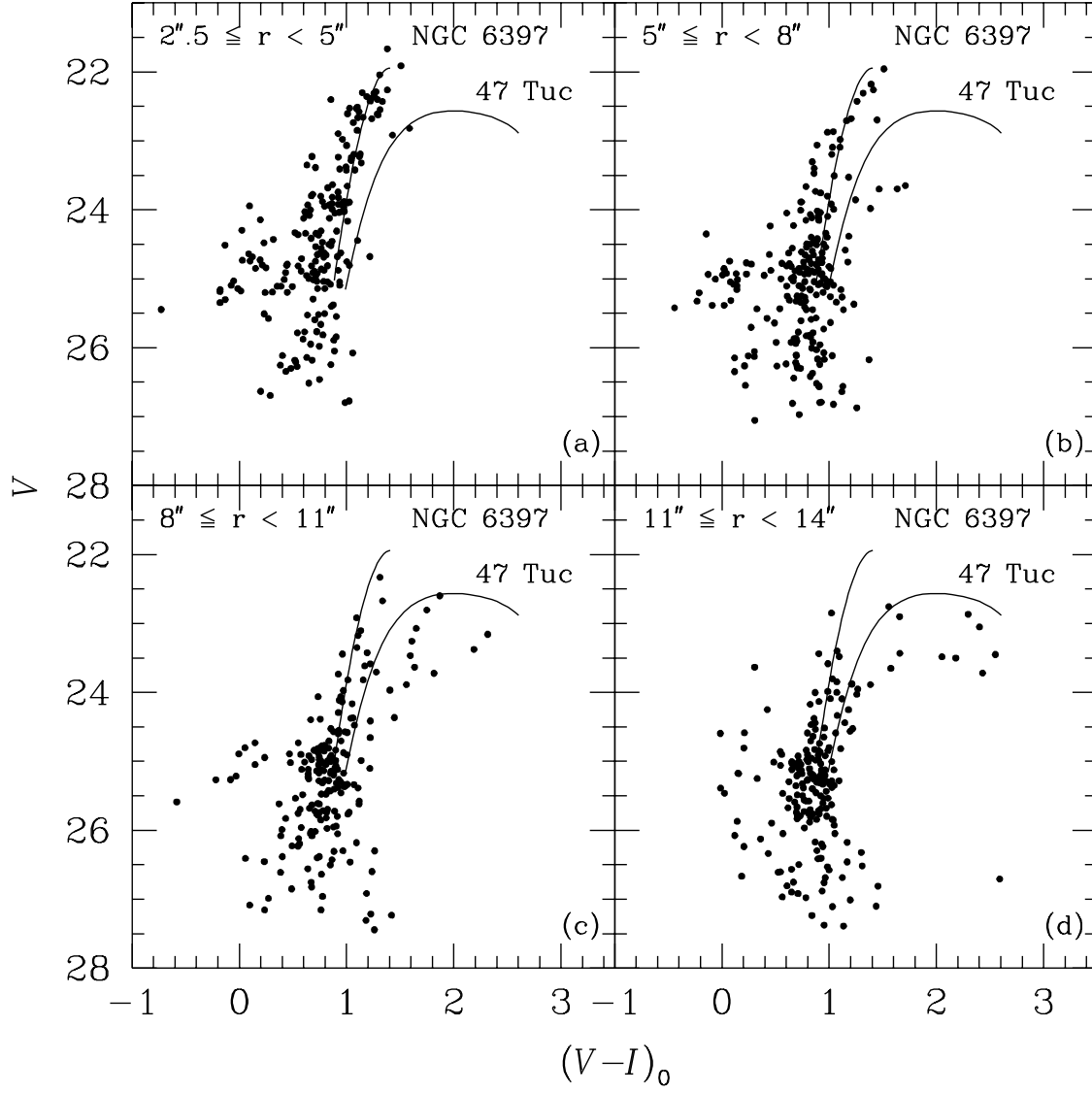


Fig. 5.— This figure shows CMDs for four annuli centered on G302. The fiducial sequences are from DCA.

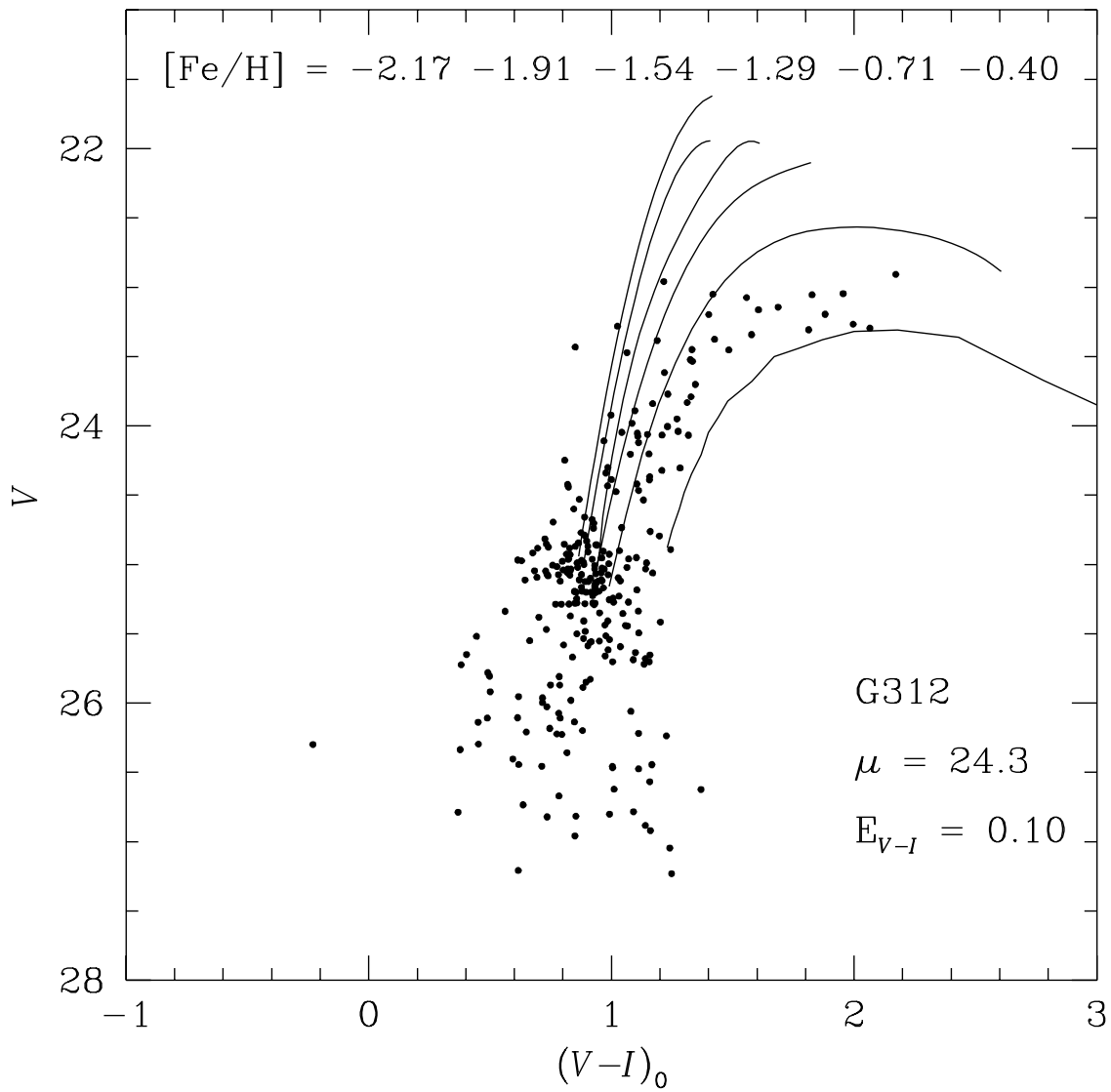


Fig. 6.— The CMD for G312. As in Figure 4 only stars between $2''.5 \leq r \leq 10''$ are plotted. The fiducial sequences are from DCA with the exception of the $[\text{Fe}/\text{H}] = -0.40$ fiducial which is from Bergbusch & Vandenberg (1992). The lack of a blue HB is consistent with G312 being metal-rich.

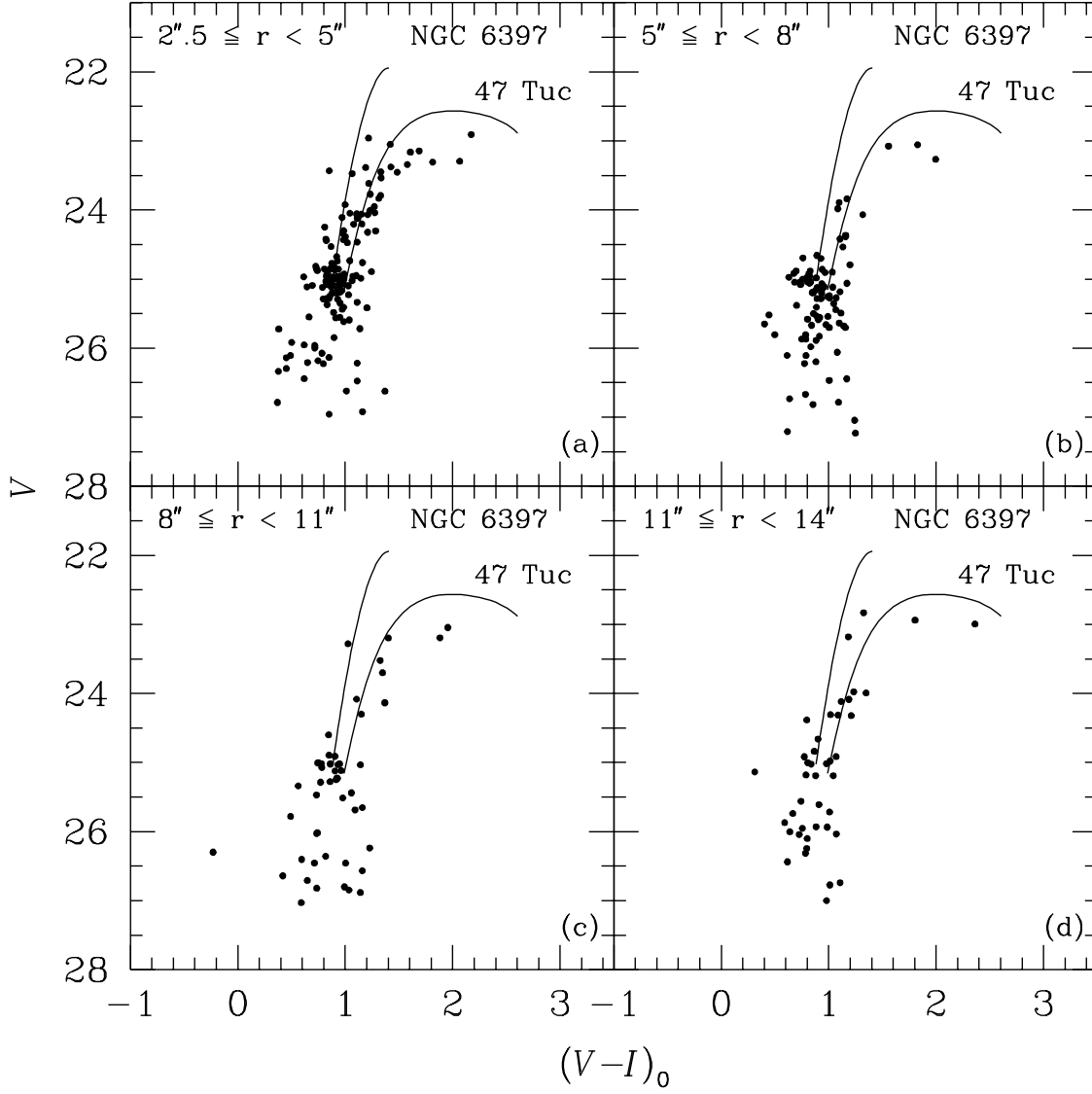


Fig. 7.— This figure shows CMDs for four annuli centered on G312. Since G312 has a metallicity similar to the mean metallicity of the M31 halo stars in the line of sight near G312 it is not possible to determine the limiting radius of G312 in this figure. The fiducial sequences are from DCA.

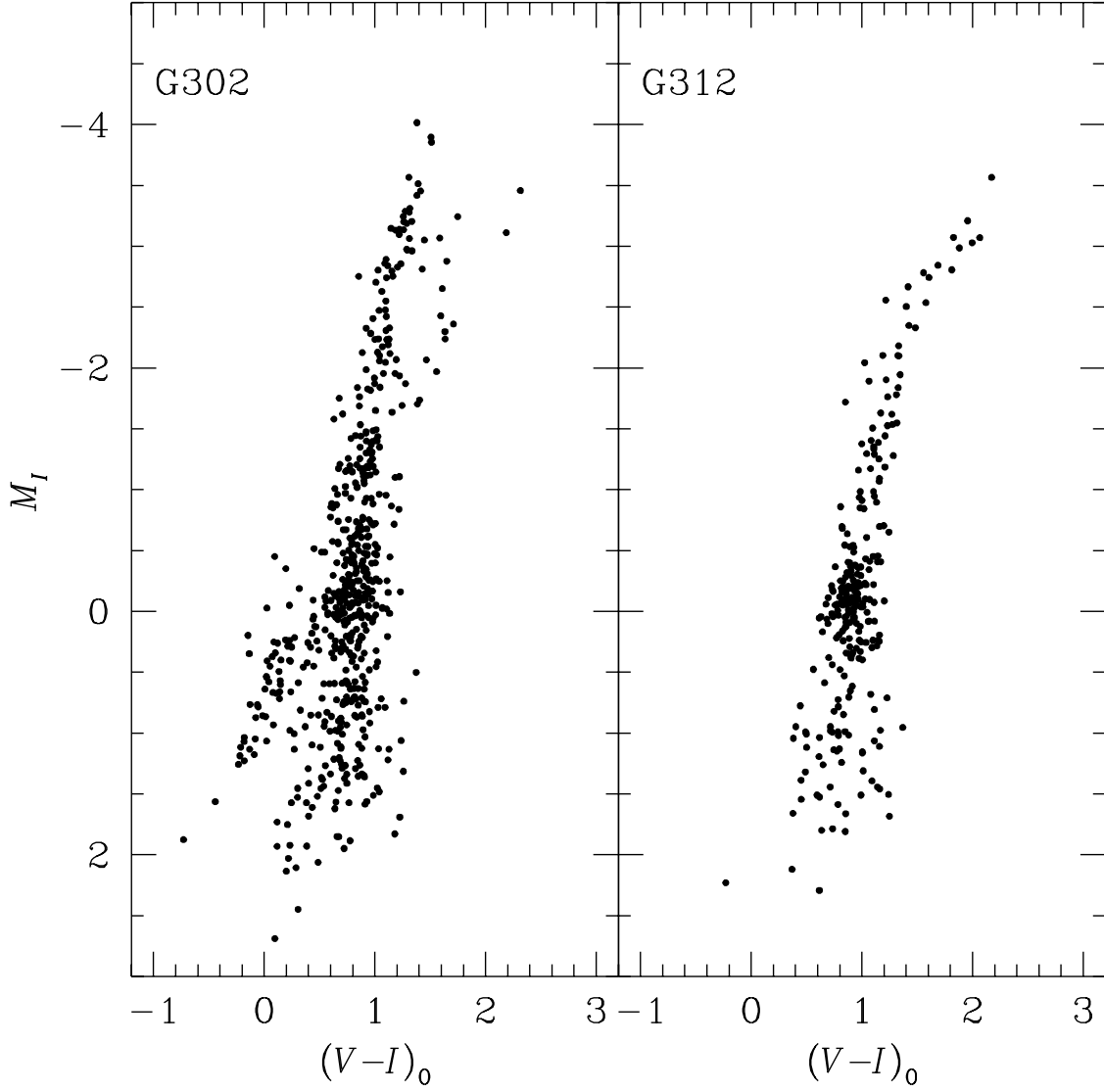


Fig. 8.— This figure shows the $(M_I, (V-I)_0)$ CMDs for G302 and G312. A distance modulus of $\mu_0 = 24.3$, a reddening of $E_{V-I} = 0.1$, and an extinction $A_I = 0.19$ was assumed as discussed in Sec. 2.2.

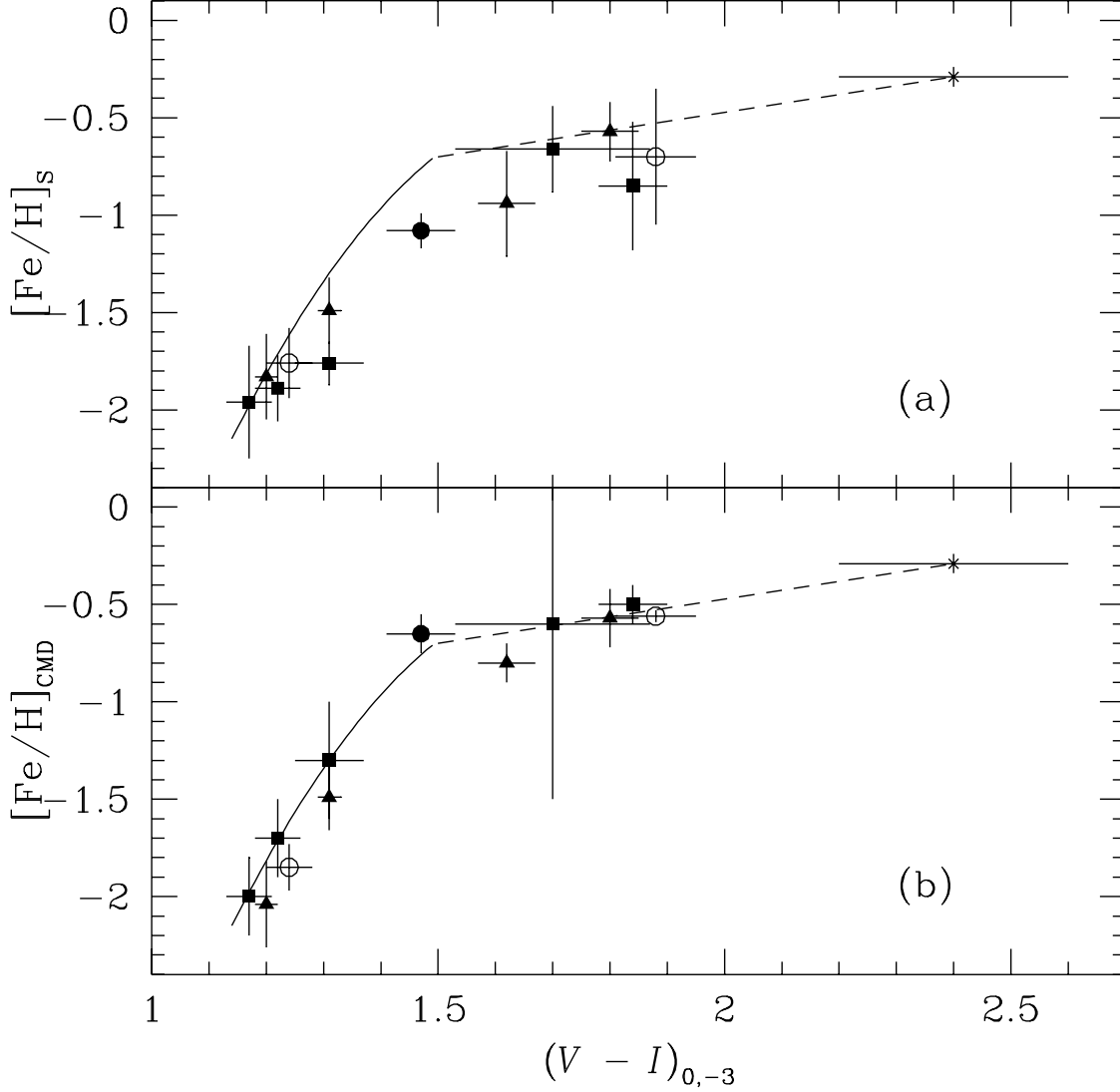


Fig. 9.— The open circles represent the data for G302 and G312 from this paper. The solid circle is data from Rich et al. (1996), the solid squares are data from Couture et al. (1995), and the solid triangles are data from Ajhar et al. (1996). The horizontal error bars only include the uncertainty due to the width of the RGB, not any uncertainties in the reddening or distance modulus of the individual GCs. The solid line shows the DCA relationship between iron abundance and the $(V - I)_{0,-3}$ color while the dashed line shows our extension to this relationship to include the metal-rich Galactic GC NGC 6553 (indicated with a “*”). Spectroscopic $[\text{Fe}/\text{H}]$ values from HBK are plotted on the ordinate of panel (a) and $[\text{Fe}/\text{H}]$ values derived from the CMDs are plotted on the ordinate of panel (b). Notice that in (b) all the GCs fall within $1\text{-}\sigma$ of the extended DCA relation except for G108, which is $\sim 3\text{-}\sigma$ redder than predicted by DCA.

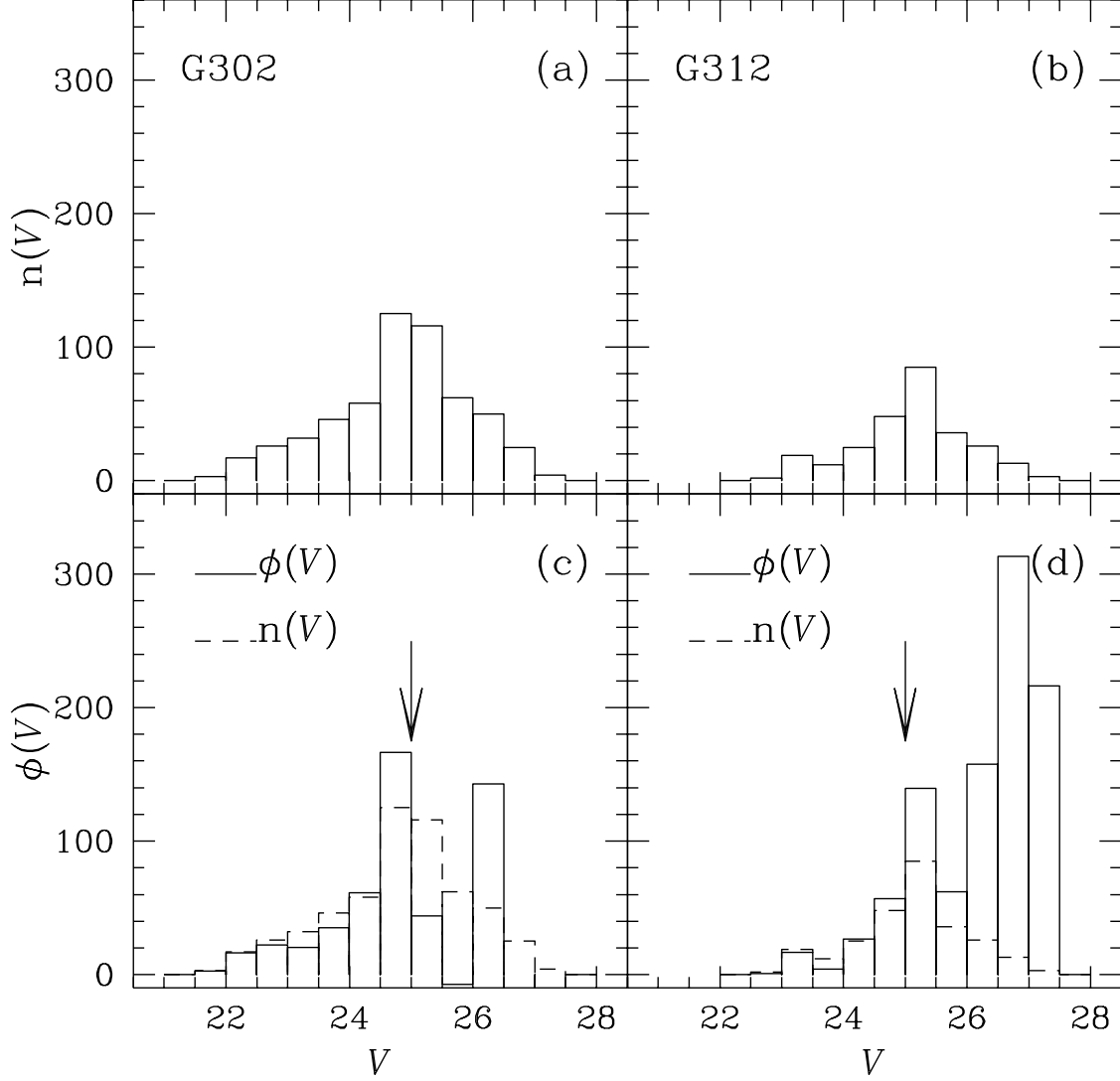


Fig. 10.— The upper panels, (a) and (b), show the observed LFs for G302 and G312 respectively. Only stars between $2''.5 \leq r < 12''.5$ were used to construct these LFs. The lower panels, (c) and (d) show the completeness-corrected LFs with the completeness-corrected background LF subtracted (solid lines) and the observed LFs (dashed lines). The completeness-corrected LFs become unreliable below the level of the HB (indicated with an arrow).

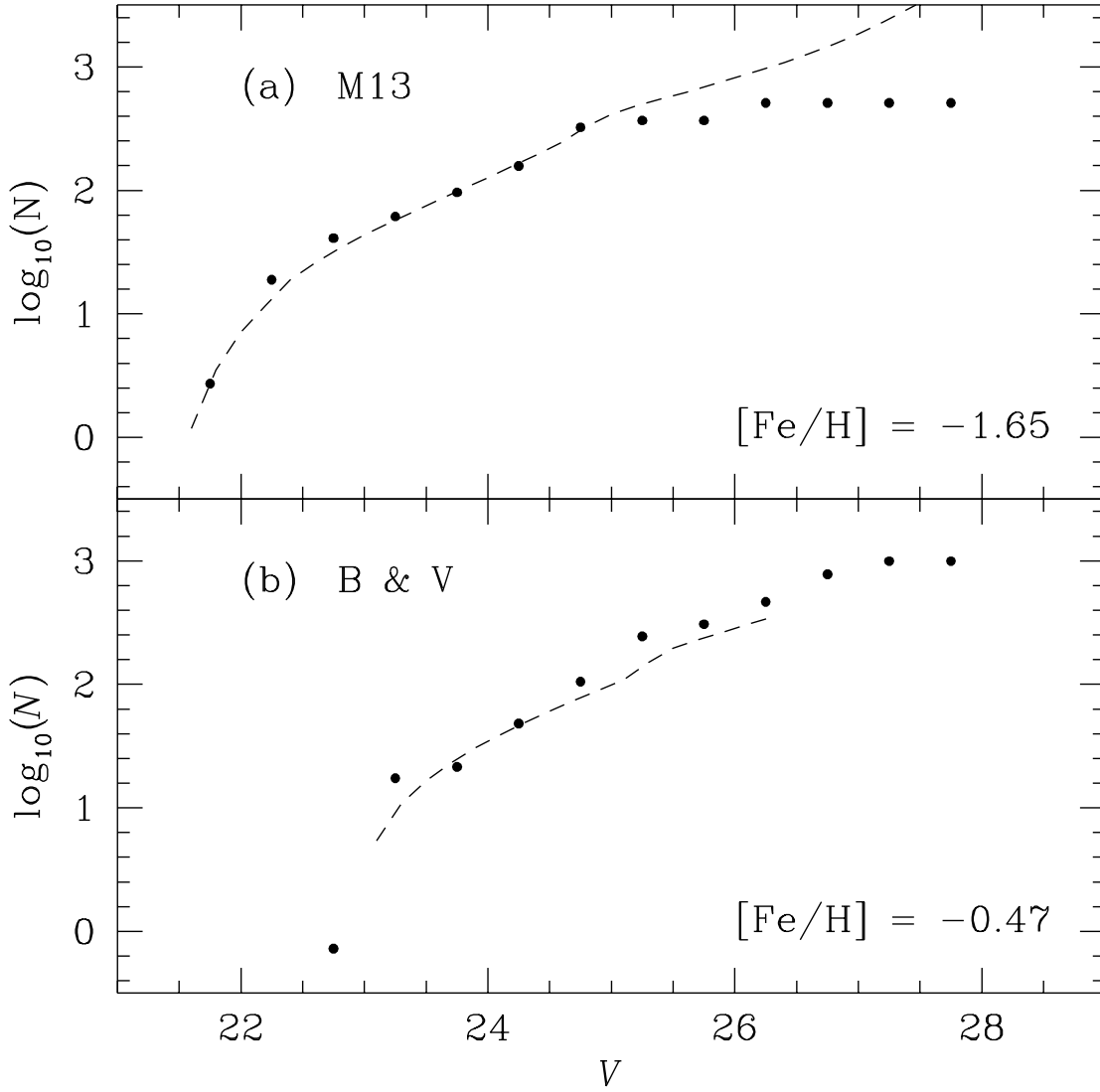


Fig. 11.— The upper panel (a) compares the cumulative LF for G302 (solid circles) to the cumulative LF of the metal-poor Galactic GC M13. Panel (b) compares the cumulative LF for G312 with a theoretical LF for an old metal-rich GC. The comparison LFs have been scaled so that they contain the same number of stars at $V = 24$ as the M31 GC LFs do.

Fig. 12.— The solid points represent the observed surface brightness profile of G302, while the open triangles in the inner $0''.1$ indicate the surface brightness corresponding to saturation for the WF3 CCD. The solid line is the best-fitting isotropic MK model and the dashed line is the best-fitting anisotropic model. The arrows indicate the tidal radii for each model.

Fig. 13.— The solid points represent the observed surface brightness profile of G312. The solid line is the best-fitting isotropic MK model and the dashed line is the best-fitting anisotropic model. The arrows indicate the tidal radii for each model.

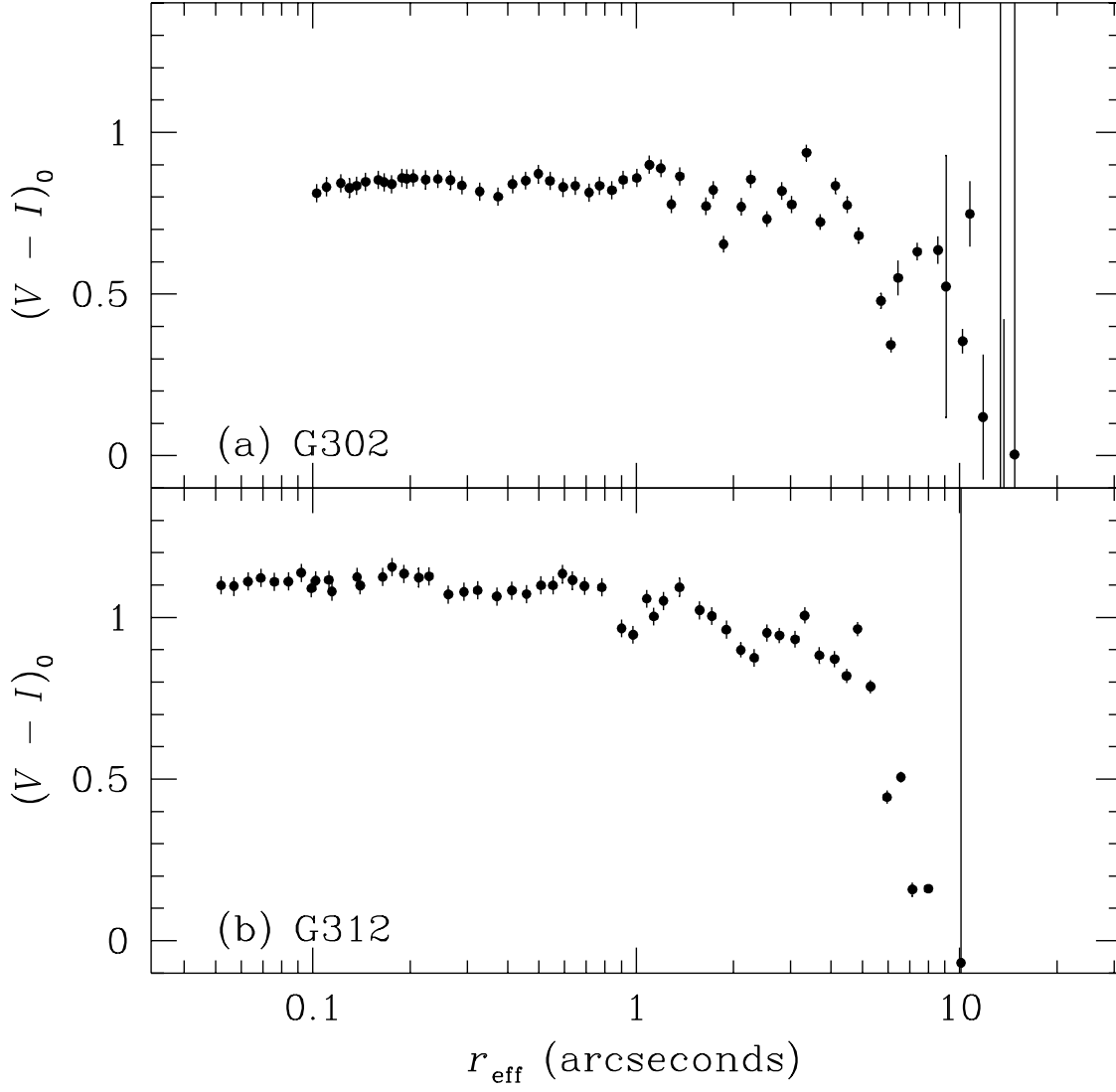


Fig. 14.— This figure shows the integrated color profiles for G302 and G312.

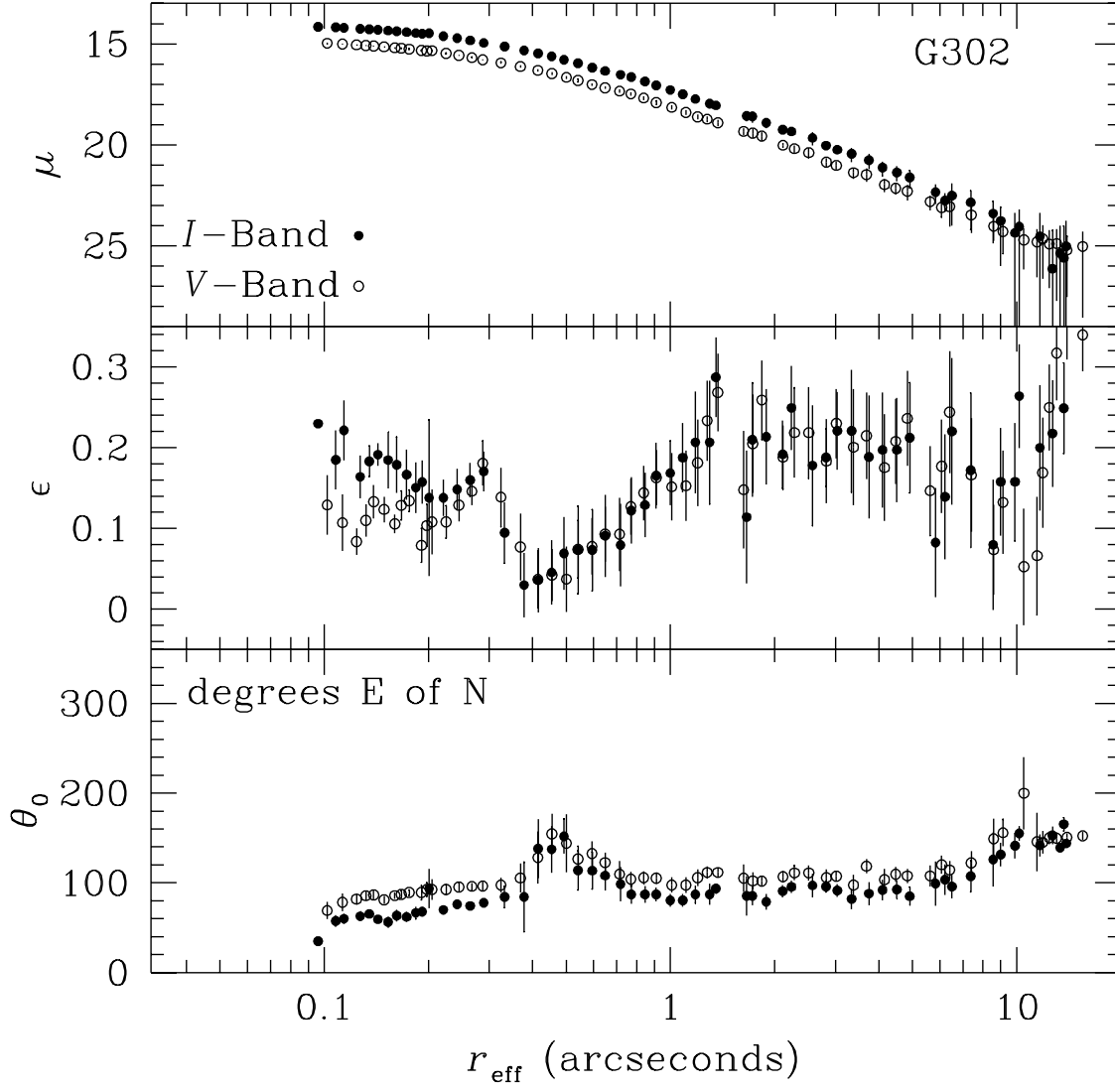


Fig. 15.— This figure shows the calibrated surface brightness profiles, μ , ellipticity profiles, ϵ , and orientation profiles, θ_0 , for G302 in the V- and I-bands.

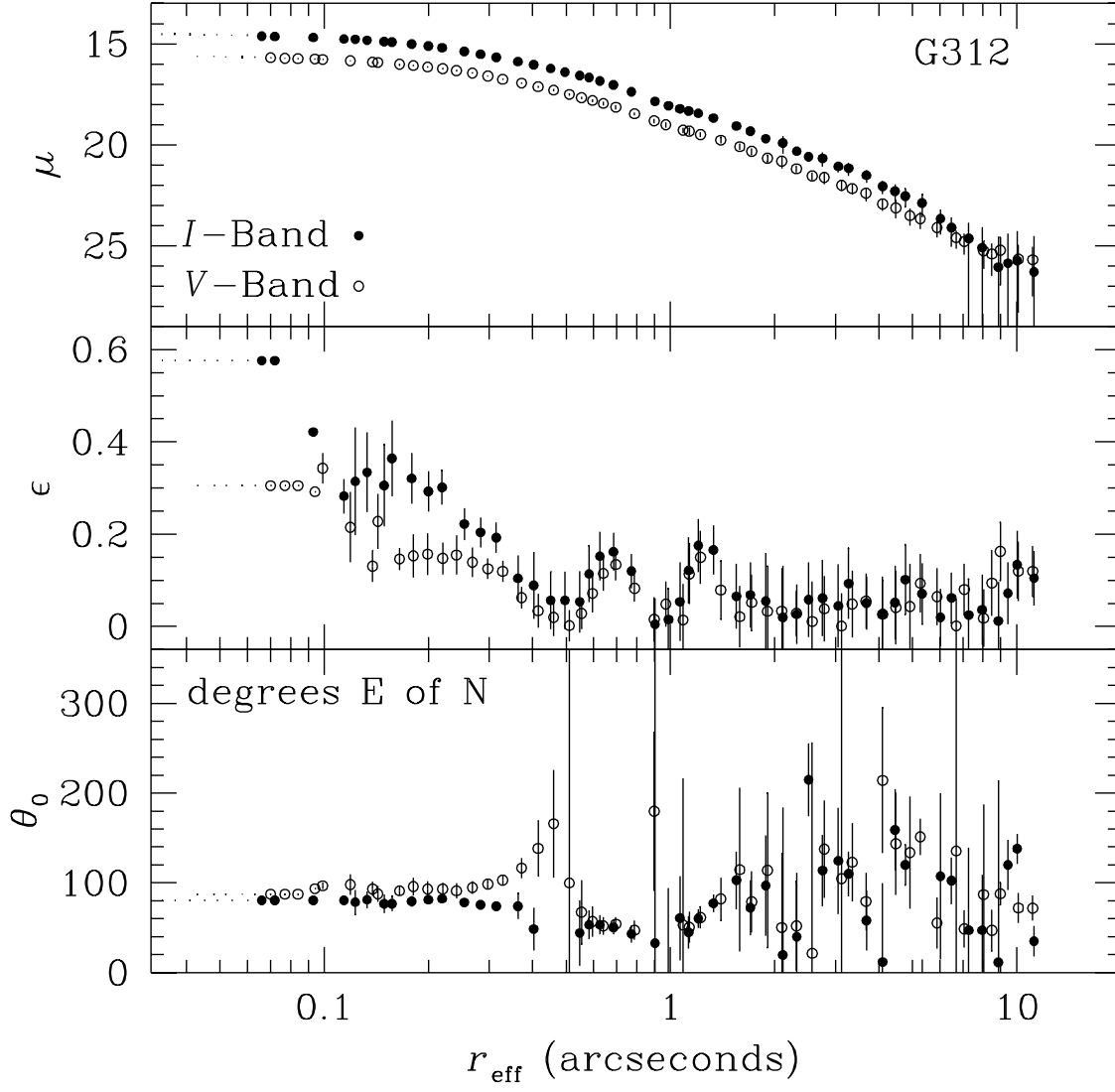


Fig. 16.— This figure shows the calibrated surface brightness profiles, ellipticity profiles, and orientation profiles for G312 in the *V*- and *I*-bands.

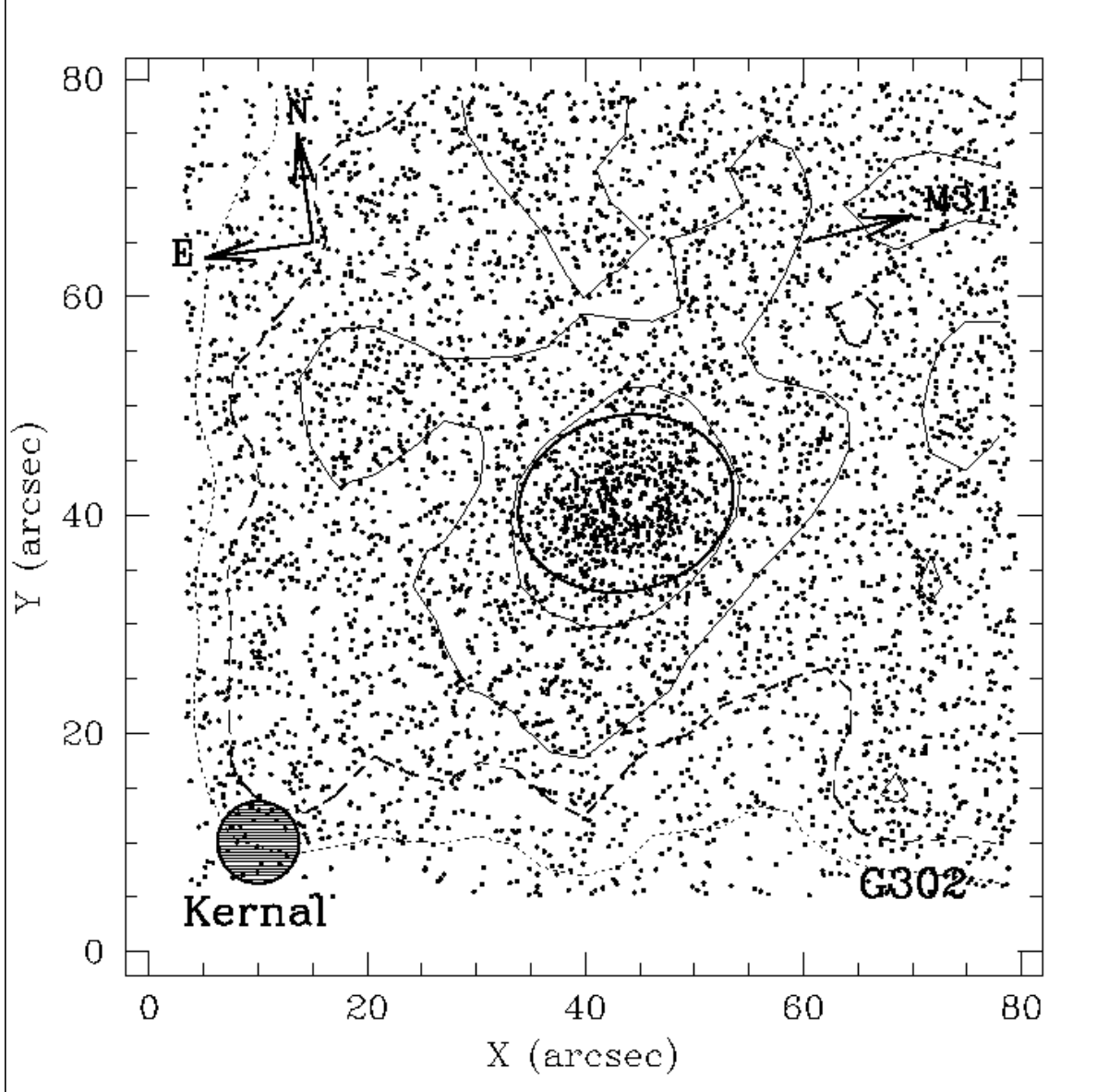


Fig. 17.— The solid ellipse has an effective radius equal to the fitted MK tidal radius for G302 and is oriented in the same direction as the GC. The dashed contour represents the surface density of stars in the M31 halo at the location of G302 ($= \Sigma_{\text{bgd}} = 0.6196 \text{ stars}/\square''$). The solid contours are $\Sigma = 0.8, 1.2 \text{ stars}/\square''$ and the dotted contour is $\Sigma = 0.4 \text{ stars}/\square''$. The outermost contours are strongly influenced by the size of the WF3 CCD. The contours inside the fitted tidal radii have not been plotted for clarity. The arrow points towards the center of M31.

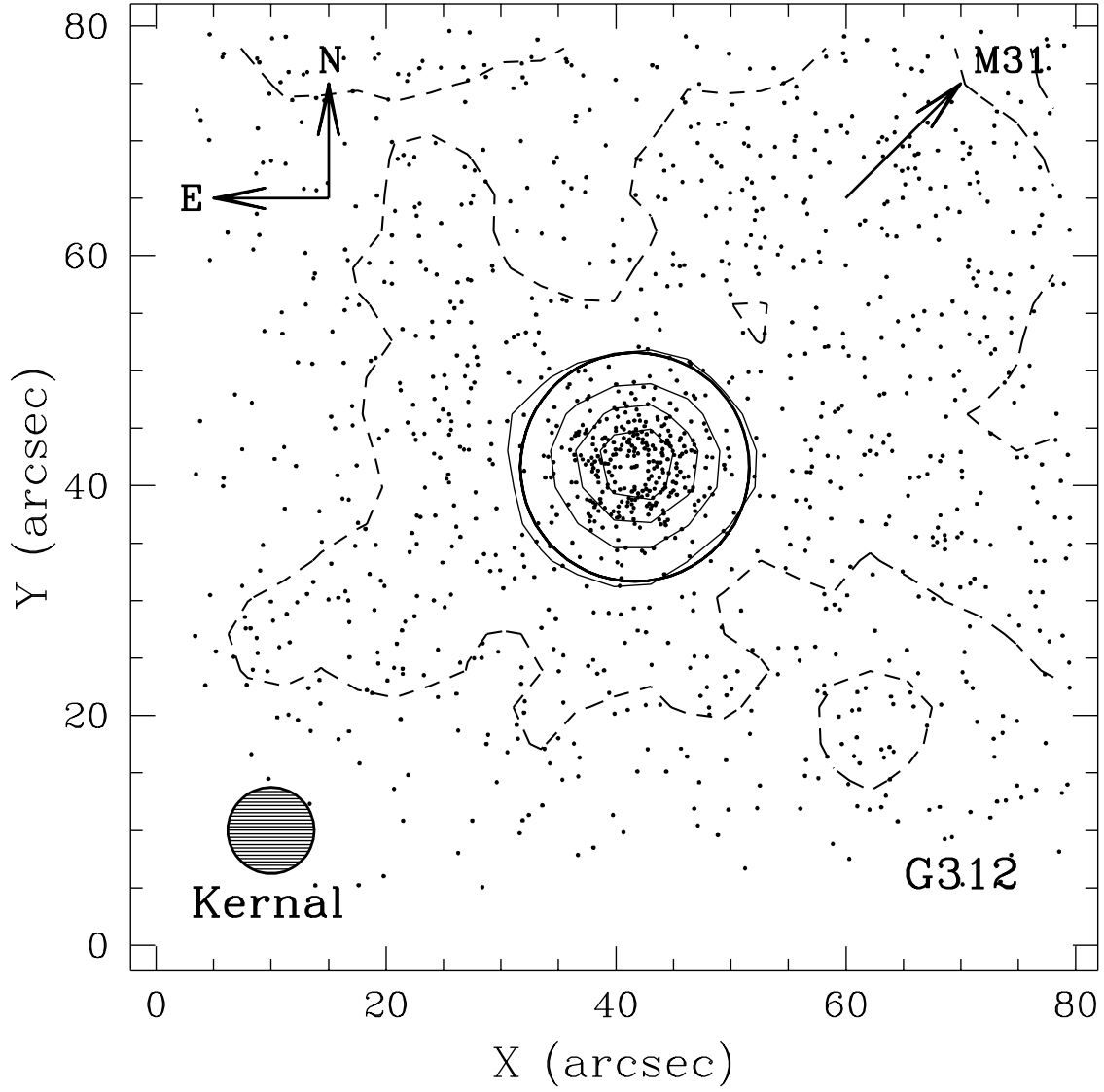


Fig. 18.— The solid circle represents the fitted MK tidal radii of G312. The dashed contour represents the surface density of stars in the M31 halo at the location of G312 ($= \Sigma_{\text{bgd}} = 0.1688 \text{ stars}/\square'$). The solid contours are $\Sigma = 0.4, 0.8, 1.2, 1.6 \text{ stars}/\square'$. The innermost contours have not been plotted for clarity.

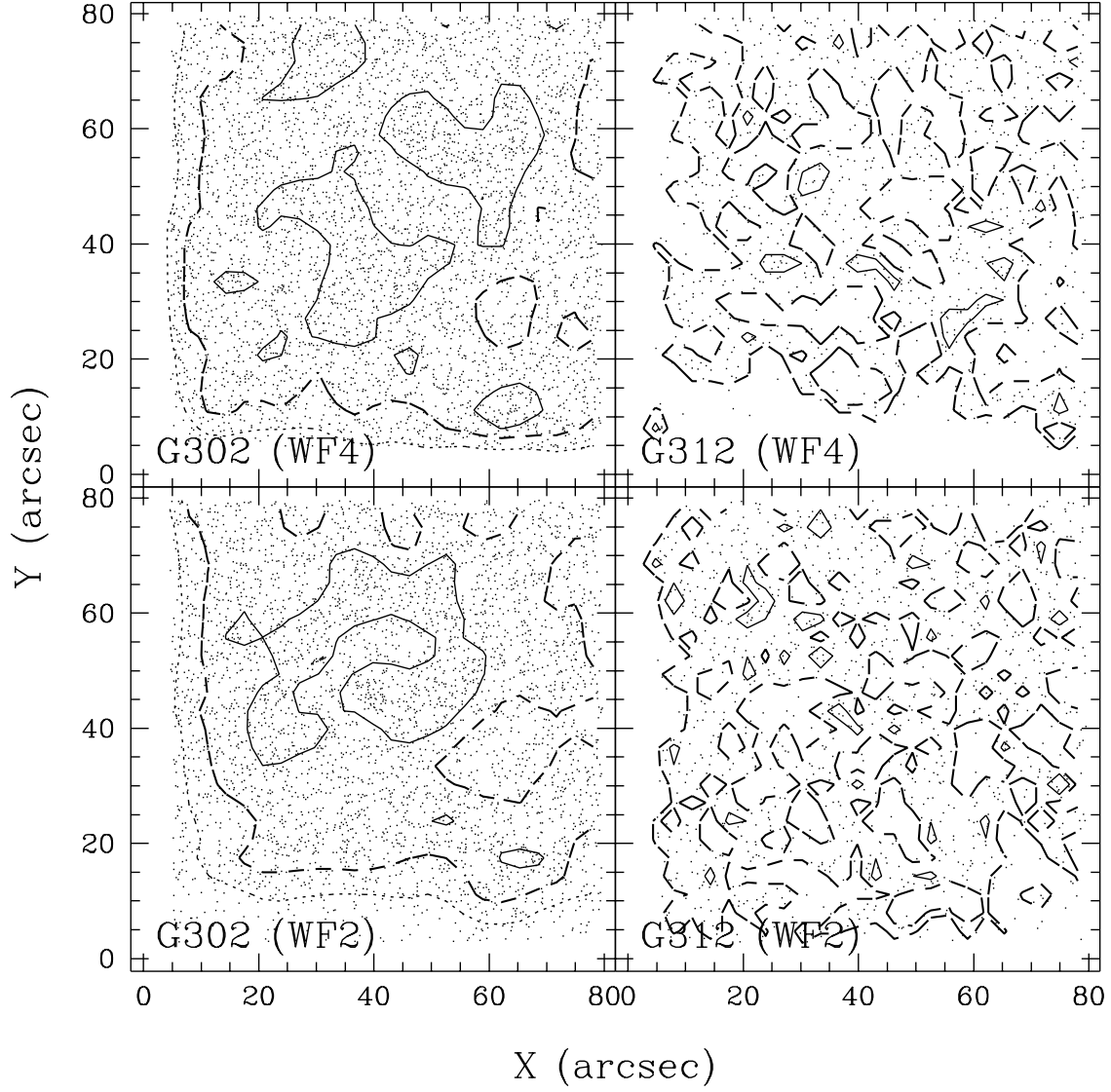


Fig. 19.— This figure shows isodensity contours for the WF2 and WF4 fields for G302 and G312. The contour intervals are the same as for Figures 17 and 18. The fields in this figure are not oriented in the same direction as the WF3 CCDs in Figures 17 and 18.

Fig. 20.— The upper panel shows the value of ζ_2 as a function of position angle for G302, while the lower panel shows ζ_2 as a function of position angle for G312. θ_0 is the angle where ζ_2 is at its minimum, which corresponds to the position angle (in degrees east of north on the sky) of the major axis of the GC. $P(\eta)$ is the probability that the observed value of η will occur by chance in a uniform distribution of stars about the GC (see Figure 21).

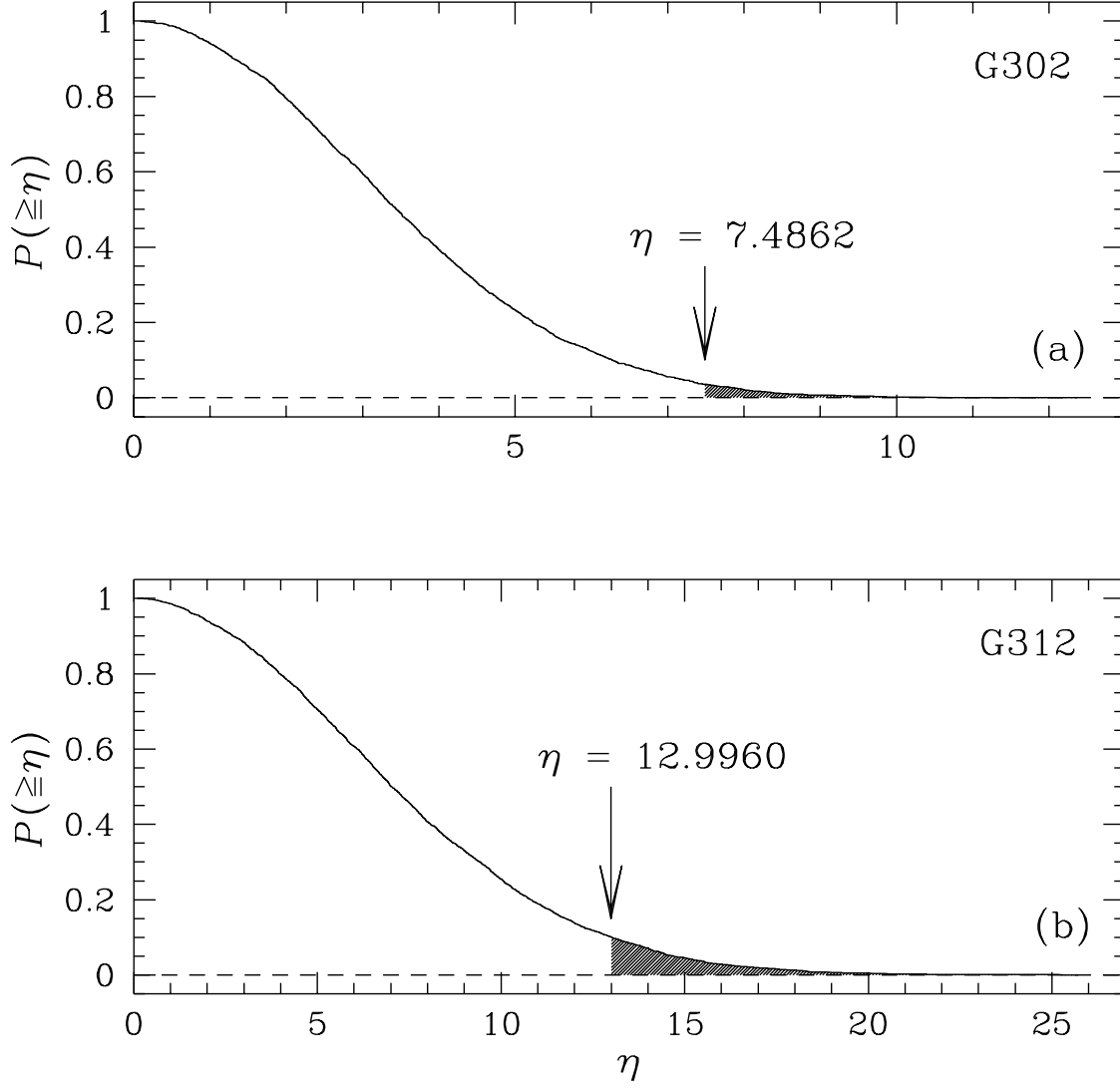


Fig. 21.— This figure shows the cumulative probability distributions, $P(\geq \eta)$, for observing a value $\geq \eta$ by chance if the observed distribution of stars was drawn from a circularly symmetric uniform distribution of stars. Panel (a) shows $P(\geq \eta)$ for the G302 field while panel (b) shows $P(\geq \eta)$ for the G312 field. The two cumulative probability distributions are different because the G302 and G312 fields contain different numbers of stars. The shaded areas under each curve represent the probabilities that values of η at least as large as those measured for G302 and G312 would be observed by chance in a uniform distribution of stars about each GC.